Three-Dimensional Simulation of Gas and Dust in Io's Pele Plume

William J. McDoniel[a], David B. Goldstein[a], Philip L. Varghese[a], Laurence M. Trafton[b]

[a]*Department of Aerospace Engineering and Engineering Mechanics, The University of Texas at Austin, Austin, TX, 78712, United States*

[b]*Department of Astronomy, The University of Texas at Austin, Austin, TX, 78712, United States*

Abstract

Io's giant Pele plume rises high above the moon's surface and produces a complex deposition pattern. We use the direct simulation Monte Carlo (DSMC) method to model the flow of SO_2 gas and silicate ash from the surface of the lava lake, into the umbrella-shaped canopy of the plume, and eventually onto the surface where the flow leaves black "butterfly wings" surrounded by a large red ring. We show how the geometry of the lava lake, from which the gas is emitted, is responsible for significant asymmetry in the plume and for the shape of the red deposition ring by way of complicated gas-dynamic interactions between parts of the gas flow arising from different areas in the lava lake. We develop a model for gas flow in the immediate vicinity of the lava lake and use it to show that the behavior of ash particles of less than about 2 μm in diameter in the plume is insensitive to the details of how they are introduced into the flow because they are coupled to the gas at low altitudes.

We simulate dust particles in the plume to show how particle size determines the distance from the lava lake at which particles deposit on the surface, and we use this dependence to find a size distribution of black dust particles in the plume that provides the best explanation for the observed black fans to the east and west of the lava lake. This best-fit particle size distribution suggests that there may be two distinct mechanisms of black dust creation at Pele, and when two log-normal distributions are fit to our results we obtain a mean particle diameter of 88 nm. We also propose a mechanism by which the condensible plume gas might overlay black dust in areas where black coloration is not observed and compare this to the observed overlaying of Pillanian dust by Pele's red ring.

Keywords: Io; Volcanism; Satellites, surfaces

1. Introduction

Large SO_2 plumes on Io were first observed by Voyager (Smith et al., 1979). They are distributed over Io's surface and many extend well above its atmosphere. Strom and Schneider (1982) first suggested that the

*Corresponding Author
Email address: william.mcdoniel@utexas.edu (William J. McDoniel)

plumes' umbrella-like structure was a result of a large, curved canopy shock. McEwen and Soderblom (1983) distinguished giant Pele-type plumes and smaller Prometheus-type plumes, and noted that the Pele-types erupt over days and leave behind red rings on the surface while the Prometheus-type remain active for very long periods of time (years) and produce white rings on the surface. They suggest that Pele-type plumes are produced by the eruptions of sulfurous gas from below the surface while the gas in Prometheus-type plumes is the result of lava flows impinging on surface frost.

Spencer et al. (2000) and later Jessup et al. (2007) strongly supported this mechanism by showing that S_2 was present in small amounts in at least some Pele-type plumes, and it is thought that the redness of Pele-type deposition rings is due to the presence of S_3 or S_4 produced in the plume (McEwen and Soderblom, 1983) or perhaps on the surface. Many plumes also produce smaller, black deposition patterns (in round spots around their source). Geissler (1999) suggests that this is silicate ash. These deposition patterns, of all colors, are not constant over time – implying unsteadiness in the plumes. Geissler (2004) discusses many of these changes over the course of the Galileo mission, including the eruption of Pillan on the east side of Pele's ring, overlaying Pele's red ring with a black circle of ash that was then covered over in turn. Williams et al. (2011) categorize the various sorts of surface materials seen on Io and summarize the literature on the silicate nature of black deposits and the contribution of S_2 or sulfur-bearing chlorides to the red color of Pele's ring.

Particle sizes and distributions in plumes are constrained by observations of scattered or absorbed light. Geissler et al. (2008) use Galileo observations to find that small Prometheus-type plumes contain about 10^6 kg of $\sim$100 nm particles, but that Pele-type plumes do not contain high densities of such particles. They note that Voyager observations in the ultraviolet produced clear images of Pele, indicating that the particles in these plumes are much smaller than the particles in Prometheus-type plumes. However, Jessup and Spencer (2012) use Hubble observations and assume a normal distribution of particle sizes to estimate gas and dust column densities to argue that Pele had a mean particle size between 50 nm and 110 nm in 1995 and between 50 nm and 80 nm in 1999. Jessup and Spencer also find that the SO_2 content of the Pillan plume could be explained by the amount of SO_2 frost present at Pillan before an eruption.

Observed features of Pele's deposition pattern, particularly the elongated shape of the $\sim$1200 km diameter large red ring and the black fans spreading out to the east and west of the vent, are hard to explain without a thorough understanding of the flow physics in the plume. Io's atmosphere is very thin, with pressures of at most tens of nanobars (Lellouch et al., 1992), so other than plasma there is little outside of the plume that could affect the gas flow. Therefore the specifics of these features must largely be encoded in the flow at the vent. Simulations can attempt to solve the inverse problem of deducing the nature of the source boundary conditions from these large-scale features by searching a weakly constrained parameter space of vent conditions.

Prior axisymmetric simulations by Zhang et al. (2003, 2004) were able to demonstrate canopy shock formation and a ring of intense gas deposition at an appropriate height and radius, respectively, using a virtual vent approach (described below) at a temperature and velocity consistent with expansion of stationary gas at 0.01 to 2 bar and 1760±210 K (stationary gas conditions from Zolotov and Fegley, 2001). Zhang et al. (2004) also showed how the presence of both small and large (10 µm) particles in the plume could explain features of the observed column density observations. Mass flux through the vent, constrained by column density observations, was found to be around 1.1×10^{29} SO_2 molecules/s ($\sim$10,700 kg/s).

These older axisymmetric calculations are valuable, but by their nature can never fully explain the asymmetric features seen at Pele. A three-dimensional calculation is necessary for these. Moreover, flow below the virtual vent was not investigated. More recently, McDoniel et al. (2011) demonstrated ring elongation caused by source geometry for colder Prometheus-class plumes, but none of the simulated deposition patterns looked much like Pele's, although they did have a suggestive absence of gas deposition along one axis of the vent reminiscent of the observed black fans. Various shapes for the vent were considered, including a rectangular slit, a half annulus, and two sources drawn directly from observations of Pele's caldera.

In this work, a new model is developed utilizing a vent geometry based on an image from Howell and Lopes (2011), and the full Pele plume is simulated with the direct simulation Monte Carlo (DSMC) method using other conditions similar to those used by Zhang et al. (2003, 2004). We present a good match to the observed red ring, explain how the source geometry gives rise to it, and discuss implications of the 3D nature of the gas flow for the interpretation of observations. We develop a model for flow just above the surface of the lava lake in order to understand gas/dust coupling at low altitudes and the importance of the lava lake's geometry for the plume flow at low altitudes. We include particles in the plume flow in an attempt to fit the black fans observed at Pele, and the observed dust deposition pattern is used in a new technique to constrain particle sizes in the plume. The line-of-sight column density images for single-size particle flows in Zhang et al. (2004) are partially reproduced in 3D, and we examine the motion of dust particles with diameters up to 10 µm in the plume flow. This gas/dust interaction is also seen to explain how continuous size distributions of dust particles give rise to the black fans on the surface.

2. Method

We simulate Io's plumes and atmosphere using the UT group's Direct Simulation Monte Carlo (DSMC) code, a previous version of which was used in the work of Zhang et al. (2003, 2004) discussed above and in atmospheric and plasma simulations by Walker et al. (2010, 2012) and Moore et al. (2009, 2012). DSMC is a statistical particle method in which the behavior of the real gas flow is obtained by extrapolation from the computed motions and collisions of a number of representative molecules (Bird, 1994). It is suitable for rarefied flows where molecular mean free paths are not insignificant relative to important flow length scales. The UT code has the ability to compute high speed molecule/ion collisions and chemical reactions, two-phase flow, droplet formation, and radiation. The code is specialized for planetary atmosphere simulations, with a spherical geometry, variable gravitational acceleration, and incorporates parameters specific to SO_2 for modeling internal energy exchange and radiation from rotational and vibrational modes. The DSMC boundary condition can also be coupled to the unsteady output of a continuum solver or another DSMC domain for modeling unsteady plume dynamics (Stewart et al., 2009 and Prem et al., 2014).

We have the ability to model dust grains as representative particles fully coupled to the gas, where gas molecules are influenced by probabilistic interactions with dust particles and dust particles experience a drag force and a heat transfer rate over each time step which is determined by the velocity distribution of the gas molecules in the DSMC cell (Burt 2003, implemented in the UT code by Morris et al. 2011). In this work, however, dust mass loading is assumed to be low, so that the dust particles have no influence on the gas flow.

Typical simulations are performed on the supercomputers at the Texas Advanced Computing Center using $\sim$1000 processors, where each processor is responsible for the simulation of $\sim 8 \times 10^5$ computational particles in $\sim 45,000$ cells.

In the course of this work, new features have been implemented to increase the speed or accuracy of the computation. As described below, processor boundaries are automatically positioned to distribute work as evenly as possible through both the transient and steady stages of a simulation. Fictitious forces arising due to the non-inertial nature of the Io-fixed reference frame were added to test their effect on ring orientation (treating the tidally-locked Io as being in uniform circular motion around Jupiter). The method for calculating the drag force on and heat transfer rate to dust particles was modified to guarantee stability and greater accuracy at all time step sizes by adapting a method for source-term linearization given in Patankar (1980); the application to DSMC was given in McDoniel (2013).

2.1. Source and Staging through Multiple Domains

The night-side Pele plume is modeled as a jet of SO_2 expanding into a vacuum from a defined source geometry (termed the "virtual vent") on the surface of a sphere. The background atmosphere is taken to be negligible due to cold night-side surface temperatures. The gas density, temperature, and velocity are taken to be uniform across the entire vent. The total mass flux is taken directly from Zhang et al. (2003), and is fixed by choosing a vent density based on the area of the simulated virtual vent. The gas temperature and velocity are chosen so as to provide a good match to the observed average deposition ring radius and canopy height, and are generally consistent with the conditions found to be suitable by Zhang et al. (2003). Notably, the flow enters the simulation domain at about Mach 3; continuum flow near the surface of the lava lake is not included in the giant plume simulations (near-surface flow is discussed in Section 2.3). This supersonic, uniform virtual vent region is discussed by Zhang et al. (2003) and is intended to reduce the computational expense of simulations by assuming isentropic expansion from some true vent conditions over

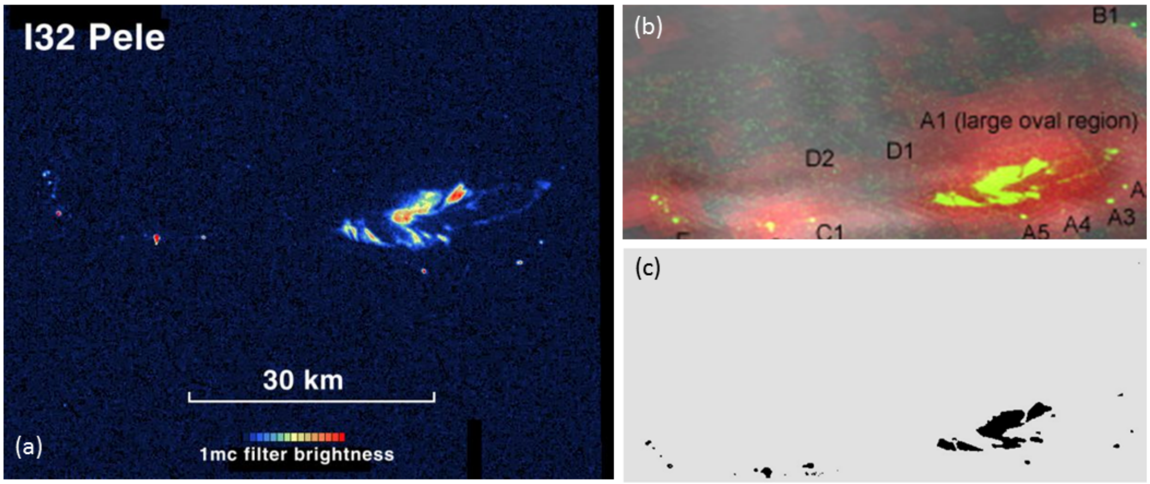

Fig. 1: (a) Galileo SSI image of Peles caldera. (b) Processed composite image of Voyager in-sunlight clear-filter observation, Galileo I32 thermal observation in red, and SSI image from (a) in green, from Howell and Lopes (2011). (c) The vent geometry used for the DSMC simulations, obtained by taking all regions of (b) with a grayscale pixel value >200 (image processed with built-in Matlab functions).

a small distance, as if the flow is expanding in a quasi-1D fashion in a diverging nozzle. The flow can also be uniformly seeded with spherical dust grains drawn from a chosen size distribution as described in Section 2.4.

The particular geometry used as the source of the plume for the DSMC simulation is drawn from Howell and Lopes 2011 (Fig. 1). Matlab was used to convert the ∼80 m resolution color image to grayscale, and ∼2700 bright pixels above a cutoff brightness were taken as the source. Uniform-property SO_2 flow (850 m/s, 500 K, 6.426×10^{-7} kg/m^3) is assumed for simplicity, and is reasonable to the extent that the actual plume emits from uniform-property lava by way of small holes or fissures which are approximately uniformly distributed across the simulated area (see section 2.3).

Inflow is created from a collection of uniform-property subsurface buffer cells. At each time-step, gas molecules are created in each subsurface cell according to a Maxwellian velocity distribution and are allowed to move freely. Dust particles are also created in the subsurface cells and are given initial velocities from a prescribed distribution (see Section 2.4). Those gas molecules and dust particles that escape the subsurface cells into the computational domain are preserved for later time steps, and those remaining behind are removed from the calculation. Molecules exiting the top or sides of a domain are removed from the simulation and recorded for use in outer domains (we record outflow over many time steps and then sample from this distribution of fluxing molecules to create inflow in the subsequent domain). The outermost domain features a large buffer cell extending to a very high altitude where collisions are not simulated. This enables cheap simulation of free-molecular high-altitude flow early in simulations before the canopy shock forms. Molecules

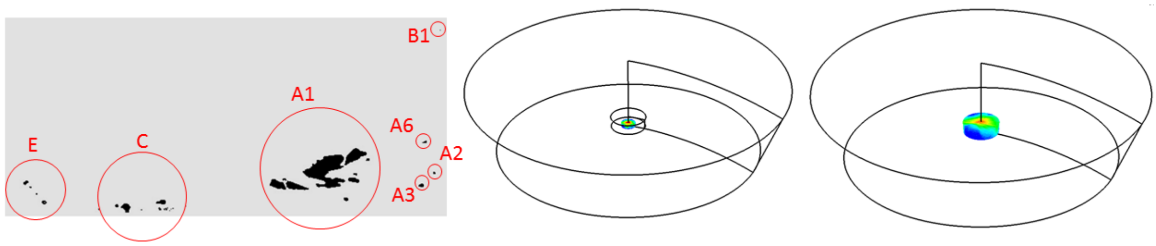

Fig. 2: (left) DSMC virtual vent with seven independent source regions circled and labeled following the convention in Howell and Lopes (2011), although note that our Source A1 includes the area where Howell and Lopes identify two more regions A4 and A5, and we identify a new area A6. Sources E, C, and A1 are simulated in 3D, with 40 m resolution of the source geometry. Sources A2, A3, A6, and B1 are treated as small axisymmetric plumes with source radii of 200 m. The center and right images show the full 1600 km diameter far-field domain, curving over the surface of Io. In the center image the first domain (up to 20 km altitude) integrating all seven source regions is visible within a wire frame of the second domain. In the right image the second domain (up to 60 km altitude) is visible.

in the outermost domain that hit the surface of Io are assumed to stick; they are removed from the simulation and recorded as deposition.

The near-vent flow simulation is computationally intensive, but since the inflow boundary condition is steady at the vent, the near-vent regions will also become steady (in our time-explicit approach) much earlier than flow farther away. Because the gas is expanding supersonically into a vacuum, flow down-stream (higher in altitude) does not influence flow upstream (closer to the vent), and the plume simulation can be split into multiple stages where inner regions are one-way coupled with outer regions. This allows simulation of the expensive inner regions to be halted while the outer regions are still developing. The DSMC source pictured in Fig. 1c is separated into seven distinct regions (Fig. 2a), each of which is simulated independently for the first 1-2 km above the surface using 64 processors each for the three large regions on the left (Sources E, C, and A1) and one processor each for the four small circular regions on the right edge (A2, A3, A6, and B1). After this, the flow is simulated using ∼1000 processors in three stages; one stage from 2 to 20 km altitude, one from 20 to 60 km, and a final stage for the rest of the plume. Time step size, grid resolution, and particle weights are adjusted across domains so as to resolve the high-density flow near the vent while simulating the entire span of altitudes efficiently.

2.2. Gas and Dust Deposition Comparisons

Several kinds of output can be obtained from the plume simulations, and simulated deposition patterns of gas and dust can be directly compared to Galileo observations. However, performing this comparison presents several challenges. As will be shown, in the simulated plume SO_2 gas falls to the surface in a ring that closely resembles the large red ring observed at Pele. For the real plume, the ring is likely produced by species such as S_3 or S_4, and the plume flow near the surface and far from the vent can be influenced by

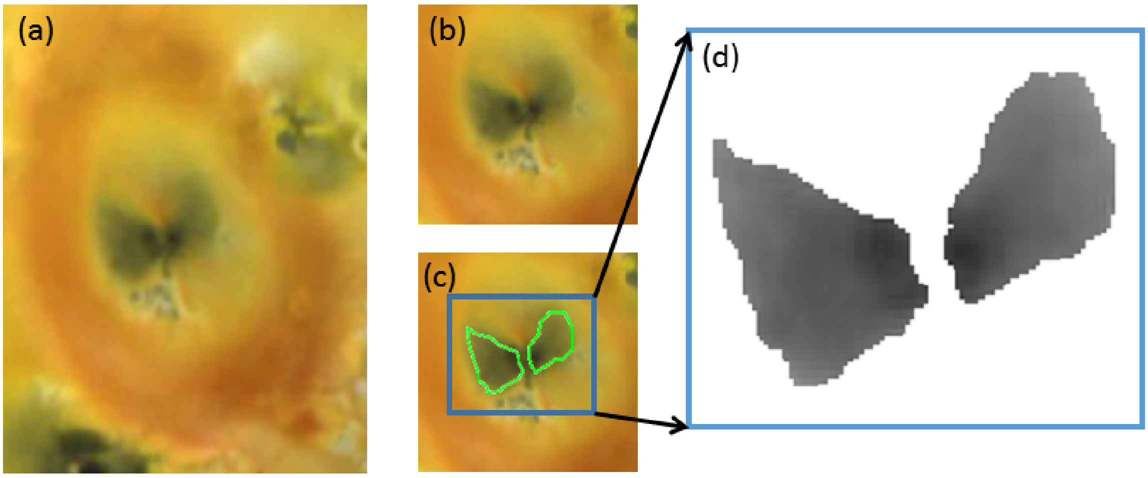

Fig. 3: (a) Galileo image of Peles multicolored deposition pattern on Io's surface. (b) A region around the plume source where we believe coloration of the surface is strongly influenced by plume activity and from which target regions for comparison will be chosen. (c) The primary target region used to compare dust deposition to simulations is colored black. (d) Close-up of the grayscale surface inside the two fans of the target only; we fit our dust deposition model to each of the 3,194 gray pixels shown.

the presence of a sublimation atmosphere during the day (Zhang et al., 2003) or by interaction with plasma in the canopy. The actual red coloration of the surface is likely to be a complex function of the relative concentrations of different materials falling to the surface, the tendency of each material to undergo chemical reactions while on the surface, and the optical properties of the resulting composite surface. Here, we only say that the long time scale of observed changes to Io's surface due to Pele – Geissler (2004) describes Pillan being covered over by Pele over the course of many months – indicates that day/night variation is not a significant contribution to surface changes. We further suggest that the effect of Pele on Io's surface is dominated by the night-side plume, which is not mediated by a sublimation atmosphere, which Zhang et al. (2003) showed can cause a gas-dynamic bounce and a much more diffuse primary ring. Then, if the red coloring is the result of other species (short-chain sulfur in the gas at the vent or S_2 which reacts after depositing on the surface, for example) that track the gas flow, the mass flux of SO_2 into the surface on the night-side can be taken to be a reasonable proxy for the redness of the surface in observations. This suggestion is supported by the remarkable qualitative similarity between the simulated gas ring and the observed red ring (shown later in Fig. 15).

The black fans to either side of Pele's vent (Fig. 3) are likely the result of a similarly complicated process. When Pillan erupted atop Pele's ring, a large amount of black silicate ash (Geissler et al., 1999) was laid down rapidly, which was then slowly covered by Pele over months. Pele's own black deposits do not appear to be associated with short eruption events; the black fans appear nearly constant in intensity relative to the large ring, despite the fact that there is surely other material (overlaying the black ash) depositing in the same locations, even if not as much as at Pillan, which lies on Pele's red deposition ring. Simulations attempting to match Voyager observations of column density suggested the instantaneous presence of small numbers of particles of up to 10 µm in the flow (Zhang et al., 2004), and Hubble observations over long time periods lead to fairly uniform estimates of mean particle sizes (Jessup and Spencer, 2012). For these reasons we treat the dust flow and eruption from Pele as a steady process.

Relatively small amounts of simulated plume gas are seen to hit the surface inside the large red ring (both in the present results and in Zhang et al., 2003), especially to the east and west of the vent (Fig. 15), and the rate at which existing deposits are overlaid by other (non-plume) material is assumed constant. We assume that only the (daytime) sublimation atmosphere acts to resurface the ground inside the ring, and that it coats the ground uniformly because there is very little plume gas above the surface in the regions of interest. This allows us to take the coloration of the surface in those regions to be a function only of the number and size of dust particles that strike the surface per unit time. A higher rate of particle deposition will darken the surface more because more dust will be present per unit depth in the surface frost deposited by the sublimation atmosphere, which is assumed to build up at a constant rate (over months; there are day/night variations). Likewise, larger particles will darken the surface more than smaller particles on a per-particle basis because of their larger cross-sections. We assume a sparse coating of dust on the surface (so that depositing dust overlays only frost and not preexisting dust deposition) and that the surface darkness is proportional to the sum of the cross-sections of all dust particles that strike the surface per unit time. These assumptions are undoubtedly oversimplifications, but they enable us to determine dust size distributions that reproduce the observed deposition pattern and which are consistent with Zhang et al.'s results.

The particular Galileo observation chosen for the comparison is shown in Fig. 3a. Distortion due to the position of the spacecraft is ignored. We identify by hand regions of the deposition pattern that we feel provide the best basis for comparison (Fig. 3c). The regions of interest are the dark black fans to either side of the vent, away from the faint orange sprays to the north and south (which may overlay some dust). In these dark butterfly wing regions we suggest that the dust dominates the plume deposition (and it will be seen that gas deposition reaches a minimum while dust deposition reaches a maximum in these regions). Matlab is used to convert the image to grayscale (0-255), and the surface darkness is measured as 255 minus the brightness of each of the pixels. Only the 3,194 pixels in the specified regions have these darkness values extracted and compared to the simulated deposition. The center of the observed image is excluded because surface coloration here is likely to be strongly influenced by unsimulated processes, such as the spewing of large slow particles or liquid lava with unpredictable velocities.

Simulated dust deposition data can be collected as described above for some hypothesized dust particle size distribution and we can determine how much of the observed deposition can be explained by the hypothesized distribution by following the process illustrated in Fig. 4. The center of the simulation is lined up with the center of the observation, and the simulation is rotated by about five degrees about its central

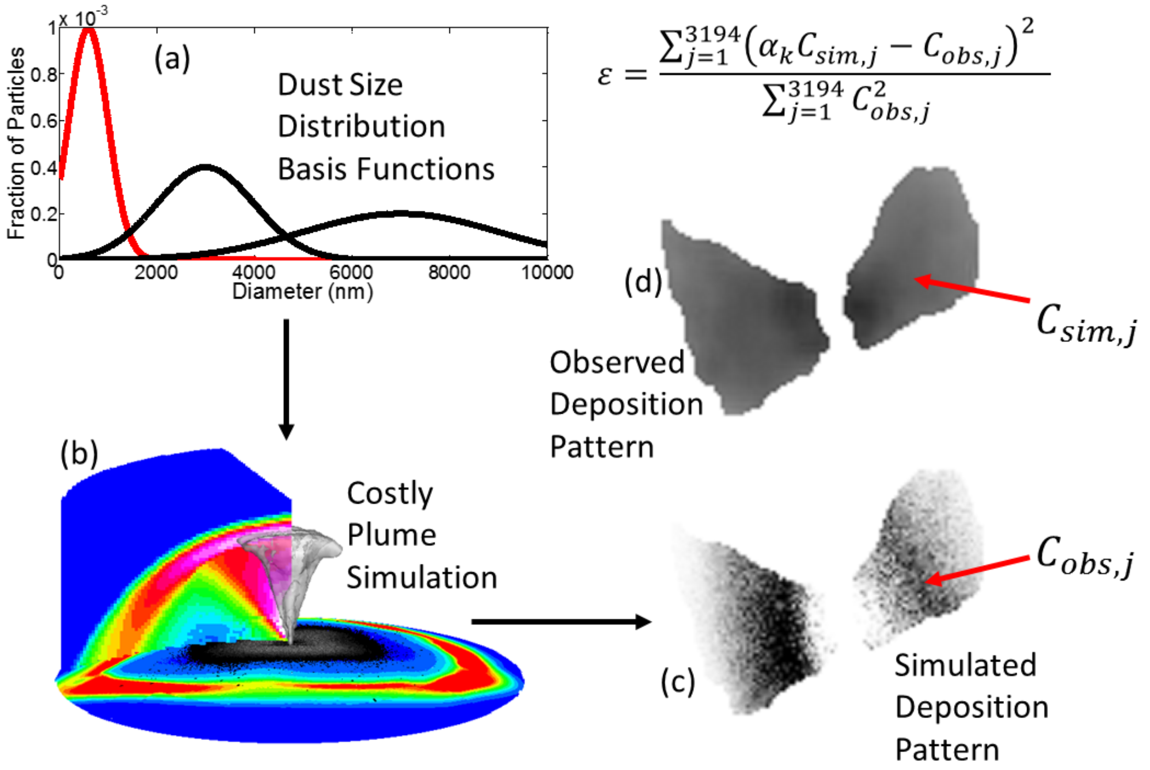

Fig. 4: (a) Sample overlapping basis functions which might be used to try to construct a best-fit size distribution are fed (b) one-by-one into the large plume simulation which yields (c) a simulated deposition pattern corresponding to each (the pattern shown corresponds to the red basis function in (a)). We then seek to find a fitting coefficient α_k for this kth basis function which minimizes the sum-of-squares error on a pixel-by-pixel (for all j) basis between the simulated pattern and the observed pattern (d).

axis to obtain a qualitatively better match of the gas rings by partially correcting for the perspective of the observation (but see the head-on comparison later in Fig. 15 where no rotation is needed). The simulated data (at a resolution of 0.3 km per pixel near the center of the domain to 3 km per pixel along the outer edges) are interpolated on to a grid of the same resolution as the observation (about 4 km per pixel) and pixels corresponding to the specified "butterfly wing" region (Fig. 3c, or a similarly-defined region) are extracted. These two vectors of data should be proportional to each other (i.e. one pixel in the simulation should be twice as dark as another pixel in the simulation if and only if the corresponding pixels in the observation also differ by a factor of two) if the simulation is accurate and if the model used to transform deposition densities and sizes to color is correct. Error in the model and Monte Carlo noise (clearly visible in Fig. 4c) prevent the two vectors from being exactly proportional, but we can perform a least-squares fit to find a best-fit proportionality constant α_k which minimizes the sum-of-squares error, and the simulated size distribution of dust particles is deemed to correspond well with observation to the extent that the least squares residual is small (i.e. to the extent that the simulated data really are proportional to the observed data). However, it is infeasible to guess at an appropriate size distribution, simulate its deposition pattern, and check whether it can explain the observed deposition. We need a method that allows us to home in on a best-fit size distribution from a relatively small number of simulations. Because our model of simulated deposition implies that the deposition pattern of the sum of several sets of dust particles is just the sum of their individual deposition patterns, we can produce a best-fit size distribution from a linear combination of basis functions that are simulated separately.

We desire a best-fit dust size distribution that minimizes the error in the simulated dust deposition, calculated in a sum-of-squares sense by taking the absolute value of the pixel-by-pixel difference between the grayscale brightness of the observation and the model brightness of the simulated deposition pattern (Fig. 4). Ideally we would use a large number of delta functions for individual basis function distributions which would span the range of interesting grain sizes, but for a given signal-to-noise ratio the computational cost scales with the number of distributions to be simulated. Therefore we simulate a small number (9-15) of size distributions that span the size range between 20 nm and 10 µm, where the upper limit is consistent with Zhang et al.'s (2004) findings that 10 µm dust can explain features seen in Voyager column density observations. These dust size distribution basis functions are simulated separately, and the resulting deposition patterns are simultaneously least-squares fit to the target data, yielding a vector of fitting coefficients (one for each basis function). These coefficients are then applied to the basis functions to obtain a best-fit size distribution. The form of the basis functions, as well as their particular means, variances, etc., are somewhat arbitrary, and this is further complicated by the non-orthogonality of these basis functions. (Even though one can choose non-overlapping basis functions in particle diameter space, the resulting deposition patterns overlap, and we are fitting using the computed deposition patterns.) We performed simulations for several choices of basis function sets and found that all produce similar results (see Section 3.2.3).

2.3. Below the Virtual Vent

As described earlier, gas enters the simulation domain at a virtual vent as a uniform-property flow at nearly Mach 3, emitting from an area derived from the Howell and Lopes temperature map. There is no variation in density, temperature, or velocity (magnitude or direction) over the virtual vent area. We now argue that this is a reasonable assumption because much more complex flow very near (within a few meters of) the actual emission surface can give rise to nearly uniform-property flow at a higher velocity and lower temperature only a small distance above the surface.

Radebaugh et al. (2004) discuss and summarize several lines of evidence suggesting that Pele is an active confined lava lake similar to, but much larger than, lava lakes on Earth. They reference the work of Burgi et al. (2002) on the Erta Ale lava lake in Ethiopia. Erta Ale has two sorts of activity – incandescent cracks and fountaining from larger holes in the crust (Fig. 5). At Erta Ale, both sorts of features are

Fig. 5: Erta Ale lava lake in Ethiopia, 80 m across and (right) Nyiragongo lava lake in the Democratic Republic of the Congo, several hundred meters across (varies). Both exhibit cracks and lava fountains. These lakes are much smaller than the lava lake at Pele, but we assume that the surface features are similar and have similar length scales.

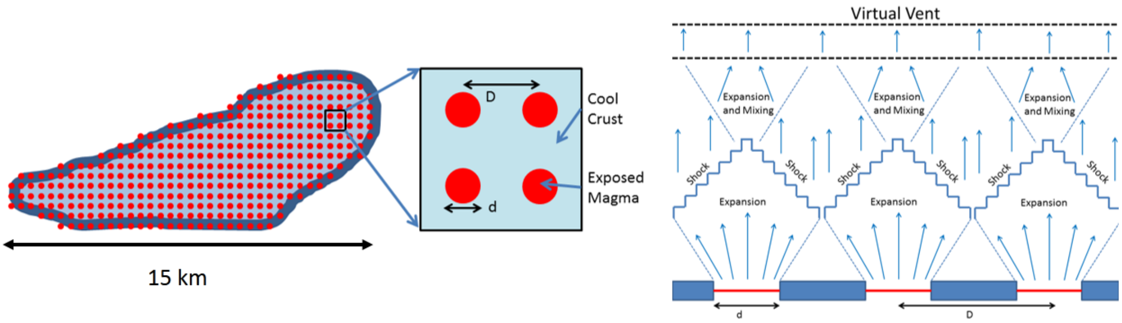

Fig. 6: (left) Drawing of large, irregular feature modeled after Source A1 from Fig. 2, covered with uniformly spaced circular sources (not to scale). The inset shows the two relevant lengths in the uniform circular source field model – the hole diameter and the hole spacing. The dark border of the lava lake is ~250 m thick on this scale. (right) Schematic of flow emerging from an infinite plane of circular sources, seen from the side.

only a few meters across (although the cracks can be tens of meters long). Radebaugh et al. argue that fountaining explains the temporal variability of the thermal emission and the higher color temperatures which are observed when Pele is viewed at an angle. Davies (2007) also argues that temporal variation in thermal observations are a result of localized disruption of surface crust, on a small enough scale to leave the rest of the lake undisturbed.

We assume that, at Pele, SO_2 escapes from the lava or is expelled from the lava from similar cracks or roughly circular fountaining regions. We assume that the gas emerges at the lava temperature and that it is nearly stationary just before it exits the lava. It will quickly (within ~1 crack width or hole diameter) expand to Mach 1 due to the extremely low ambient pressure. If the gas is venting in this fashion, the crust will act as a gas dynamic throat, and under-expanded Mach 1 gas will rise from the surface with a roughly

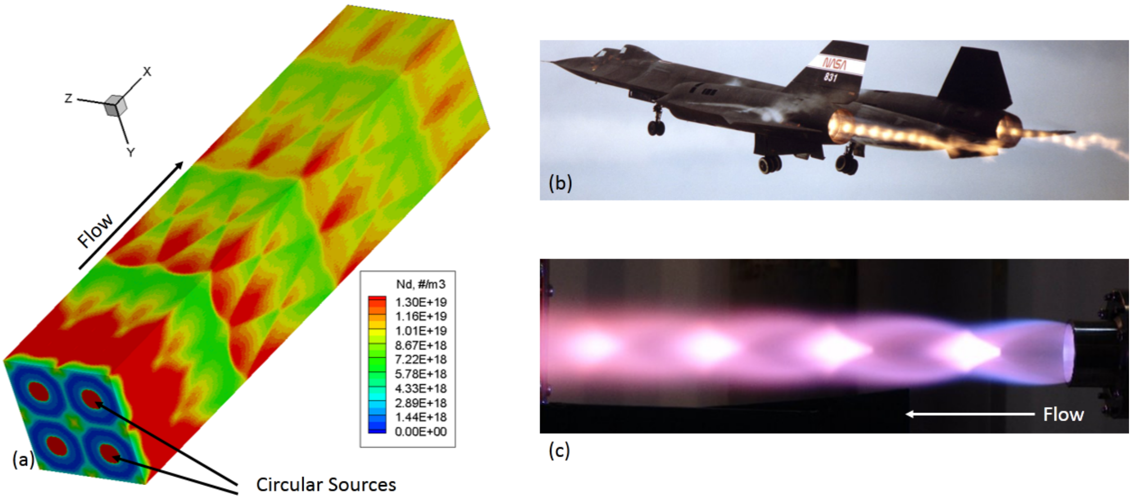

Fig. 7: (a) Density contours for SO_2 gas emerging into a vacuum from an infinite plane of circular sources at Mach 1, expanding supersonically upwards. Four sources are pictured, with contours drawn on two of the domain's symmetry boundaries. Shocks and expansions in the gas flow strongly resemble shock diamonds typically seen in under-expanded supersonic jets in the atmosphere such as in (b) and (c). (b) Shock diamonds behind the engines of an SR-71B. (c) Shock diamonds in a jet at the Swiss Propulsion Laboratory.

vertical velocity.

The lava lake at Pele is orders of magnitude larger in area than terrestrial lava lakes, but small-scale features on its crust should not depend on the size of the lava lake. Local regions of freshly exposed lava at Pele should be about as large as similar features we see on Earth. This is supported by the failure of observations to resolve such features, even at ∼30 m/pixel (although note that an October 1999 Galileo SSI image clearly indicates a long border region of the lava lake, but that McDoniel et al. (2011) show that gas emission from this elongated fissure cannot explain the observed deposition ring). Therefore, if Pele's crust is qualitatively similar to terrestrial lava lake crusts locally, it will be covered by an enormous number of features which are very small on the scale of the lake as a whole. For simplicity, we model the lava lake using uniformly spaced circular holes of gas-emitting liquid lava (Fig. 6), although similar results are achieved using a crosshatch pattern of uniform thickness cracks with uniform spacing. Because the hole diameter and spacing are so small on the scale of the lake and plume, gas emerging almost everywhere from the lava behaves as if it is expanding from an infinite array of round holes in an infinite plane of crust (this is demonstrated below). Therefore we ignore edge effects, and this enables us to take advantage of the symmetry of the problem; we simulate only one fourth of one square of crust around a circular vent, using specular boundary conditions on the side walls of the DSMC domain.

In these simulations (Fig. 7a, Fig. 8), gas expands out from the circular vents. The flow is expanding into a vacuum directly above the vents, but gas expanding laterally (parallel to the surface) encounters gas

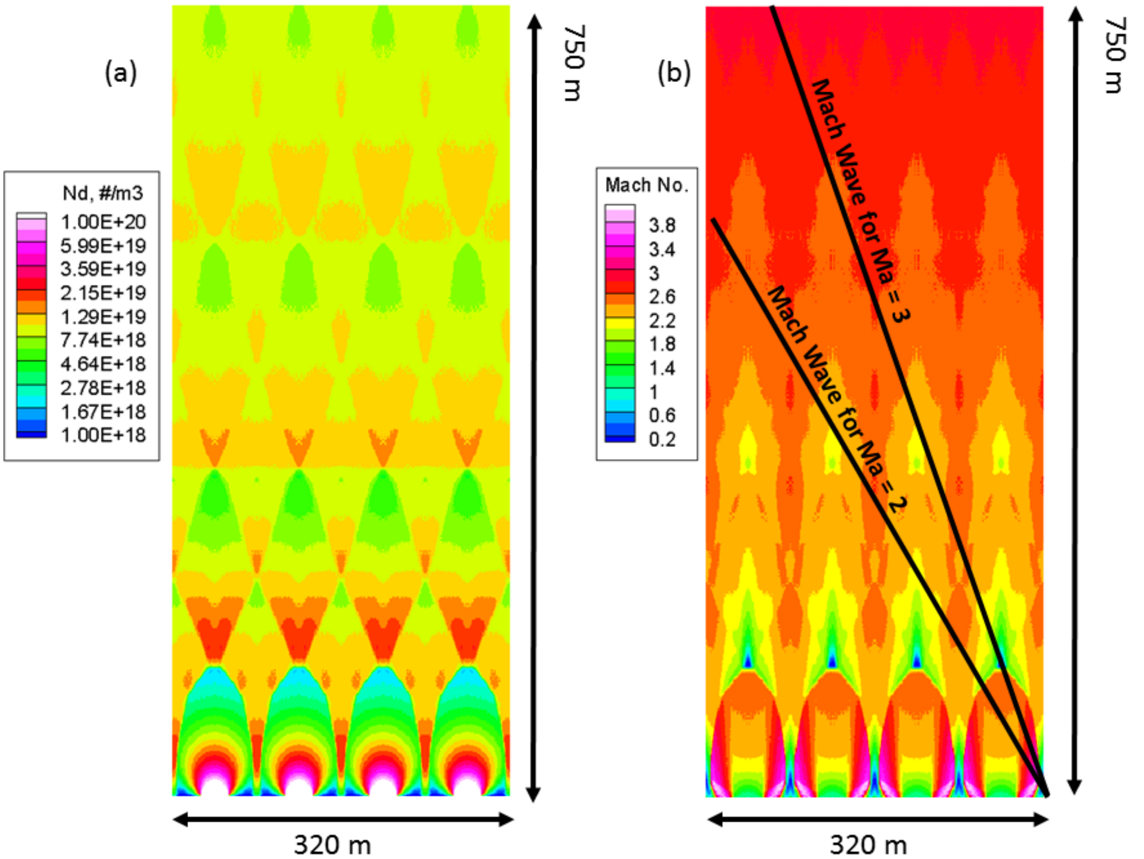

Fig. 8: (a) Number density contours for a uniform flow of SO_2 rising from an infinite plane of circular sources at approximately Mach 1 (2.73×10^{-5} kg/m^3, 1333 K, 465 m/s), which quickly expands to around Mach 3. The shocks are initially strong, but viscosity has driven the flow nearly uniform by 750 m above the vent. (b) Mach number contours for the same flow. Mach waves for Mach 2 and 3 flow are drawn from one edge of the simulation to qualitatively show the possible influence of the edge of the lava lake on the actual flow below the virtual vent.

from other circular sources. Streamlines converge above the center of regions of non-emitting crust and the flow shocks. These shocks propagate out from the regions above the cool crust and meet above the holes, where expansion begins again. This strongly resembles the shock diamonds seen when supersonic jets exhaust into a background atmosphere (Fig. 7b, c) and the physical explanation is similar except that the expansion waves are reflecting off a symmetry boundary rather than a contact surface. Rarefaction effects do not appear to be important in this near-surface region for reasonable gas densities (the Knudsen number, the ratio of the gas mean free path to a length scale, based on the hole diameter at the surface is 6×10^{-5}, and the Reynolds number, the ratio of inertial forces to viscous forces, is about 6700). The DSMC calculation is somewhat under-resolved, but the quantitative influence of the spatial resolution on observables is small. In the zero viscosity limit, this diamond pattern would persist indefinitely. With non-zero viscosity, and especially if the flow is turbulent, the shock diamonds dissipate and the flow will eventually become laterally uniform. For our virtual vent assumption to be valid, the flow must become uniform at a low enough altitude for the edge of the lava lake to be ignorable, and the flow must become uniform with properties consistent with the virtual vent used in our simulations. Ignoring radiative losses in the dense near-surface gas, the altitude at which the flow becomes roughly uniform should depend only on a Reynolds number and a length scale. Calculating the Reynolds number (either based on the hole diameter or spacing) requires a flow density and velocity at the holes. To obtain these, we refer back to our model of nearly stationary gas expanding to Mach 1 over a very short distance just above the lava. The flow velocity at Mach 1 is assumed to be consistent with isentropic expansion of SO_2 from the lava temperature. For the simulation shown in Fig. 7, the gas velocity and temperature at Mach 1 are 465 m/s and 1333 K. This is reasonable if nearly-stationary gas just above the lava surface is in thermal equilibrium with lava at $\sim$1500 K, since this is the stagnation temperature of the Mach 1 gas (stationary SO_2 gas at 1500 K which is allowed to adiabatically expand will reach the Mach 1 conditions given). Given this velocity, a hole diameter and spacing, and total lake area (from Fig. 1c), gas density is fixed by a desired mass flux.

Hole diameters can be estimated from terrestrial lava lakes, such as the Erta Ale lake (Fig. 5a). Here, diameters appear to range from meters to at most a few tens of meters. Hole spacing too can be very roughly estimated from Fig. 5a, but there are three other ways to constrain the spacing by constraining the area ratio (of gas-emitting surface area to total lava lake area). First, if the flow is to expand to approximately the virtual vent conditions by some low altitude, the area ratio must be large enough to prevent the flow from becoming uniform at a higher Mach number than the virtual vent Mach number of $\sim$3. For uniformly spaced circular holes as in Fig. 7a, the area ratio is just $\pi d^2/4D^2$. The virtual vent Mach number is somewhat arbitrary, but it cannot be too high or the plume would look radically different. This consideration suggests that the area ratio must not be much less than about 0.1; an area ratio of 0.2 would allow Mach 1 flow to expand isentropically to Mach 3 (although the flow here is not really isentropic). Second, if hot cracks or fountains dominate thermal emission from Pele, the total emitted power is determined by the area ratio and the size of the entire source region. For an average lava temperature at the gas stagnation temperature of 1500 K (the upper range of estimates from the literature, such as McEwen et al., 1998, Davies et al., 1999, and Zolotov and Fegley, 2000, cluster around 1450 K, so this is not very far off) and emissivity of 0.9, our 20 km^2 source region emits the 230 GW found by Davies et al. (2001) if there is an area ratio of 0.045. This area ratio yields a total hot surface area of 1.14 km^2, which is right in the middle of the 0.4 to 1.6 km^2 range given by Davies (2007) for 1400 K emission. In a third approach, using the results of Zolotov and Fegley (2000) for the pressure of emitted gas (which they find to be between $10^{-4.74}$ and $10^{-5.42}$ bar), our assumed mass flow rate and vent temperature require area ratios of $\sim$0.05 – 0.5.

These estimates for the area ratio ($\pi d^2/4D^2$) all agree to within about an order of magnitude, and we chose an area ratio of 0.1 for some example simulations. This area ratio implies a vent gas density of about

4×10^{-5} kg/m^3 and a hole spacing of $\sim$52 m for holes $\sim$28 m diameter (we choose to err on the side of larger length scales). Example simulations using these parameters produce gas flows which are nearly uniform by 750 m altitude (Fig. 8), justifying the virtual vent assumption and our use of Mach 3 flow at the virtual vent. The bulk of the flow quickly expands to between Mach 2 and Mach 3, which justifies the assumption that the gas below the virtual vent behaves as if it is emerging from an infinite lava lake. This is due to the nature of supersonic expansion. Information (such as the location of the edge of the lava lake) only propagates through a flow at the speed of sound, so in supersonic flow the upstream gas (gas close to the surface, in this case) is uninfluenced by downstream conditions. The flow only "sees" the edge of the lava lake once it has reached the altitude at which it intersects a Mach wave drawn from the edge of the lava lake, where the Mach angle is $\mu = \arcsin(1/M)$ for some Mach number M. Some characteristic Mach waves are drawn in Fig. 8b to show that almost all of the flow below about 750 m altitude can be treated as emerging from an infinite lava lake. The flow is supersonic nearly everywhere and above Mach 2 above about 200 m altitude. This means that edge effects are only potentially important within about 320 m of the edge of the lava lake. This distance (and the altitude at which it becomes reasonable to speak of a virtual vent) will be smaller if the surface features at Pele are smaller than simulated here. Therefore treating the flow beneath the virtual vent as emerging from an infinite lava lake is justified.

2.4. Dust Inflow Conditions

This model of the flow just above the lava lake can also be used to inform the input conditions for dust at the virtual vent. For simulating dust in the giant plume, we need a boundary condition at the virtual vent that gives the dust velocity distribution (perhaps as a function of particle size). Here, we argue that models based only on gas conditions at the virtual vent tend to overestimate the velocities of large particles. A consideration of the flow of dust below the virtual vent is necessary to constrain the vertical and (especially) tangential velocities of dust particles as they enter the giant plume simulation domain.

Fig. 9a compares the vertical velocity of dust particles at the virtual vent as a function of particle diameter for three different "equilibrium" models of dust velocity. By assuming that all dust is entrained at the gas velocity at the virtual vent (850 m/s), we are likely to greatly overestimate the speed of heavier dust particles, since all particles come from the lava lake and drag from the expanding gas is insufficient to entrain heavy dust. Assuming that grains are at terminal velocity in the gas at the virtual vent, with drag and gravity balanced so that the dust is not accelerating, is also likely to produce errors (this still yields an upwards velocity because the gas velocity is so high) because the system is not actually in equilibrium in this sense. The heavy dust does not have time to reach terminal velocity as it rises because the gas is accelerating so quickly. Instead, we directly simulate the flow of dust below the virtual vent. We use the steady gas flow-field (Fig 7a, 8) and seed dust in the circular vents shown in Section 2.3, allowing it to travel up to the virtual vent altitude while experiencing drag from the gas. Dust that escapes the top of the 750 m domain is sampled, and from these samples we infer a velocity distribution function for dust at the virtual vent, which varies with particle diameter. We then sample from this velocity distribution when creating dust particles at the virtual vent for the giant plume simulations. The mean of this "Circle Model" distribution as a function of particle size is also shown in Fig. 9a. For almost all particle sizes, these mean velocities are lower than the velocities from either of the models which used only information at the virtual vent. Dust velocities overshoot the virtual vent velocity slightly at small particle sizes, mostly because the "Circle Model" expands slightly too much and is not fully uniform at 750 m, but this is unimportant because these small particles are still coupled with the gas at the virtual vent and quickly decelerate in the large plume simulations.

As mentioned above, we initially chose to model the dust as fully coupled with the gas at the circular vents. Dust was created at the bulk gas vertical velocity of 450 m/s with zero tangential velocity. However, as seen in Fig. 9a this model led to significant slip of $\sim$350 m/s between the vertical velocities of the bulk gas flow and heavier dust particles at the virtual vent. Decoupling of the vertical velocities suggests that decoupling of velocity tangent to the surface is possible as well. We also find that the simulated line-of-sight integrated column densities for heavier dust are pencil-thin and do not compare well with the Voyager observation (Fig. 22a) when particles are introduced at the virtual vent with no tangential velocity. While the gas flow above the virtual vent is dense enough to strongly influence small particles, large particles can be almost entirely decoupled from the gas flow at the virtual vent such that they rise and fall almost ballistically in the plume simulation, so that if they begin at the virtual vent with no tangential velocity they rise straight up before falling back down on top of the lava lake. Large particles must therefore have some tangential velocity at the virtual vent, which the model of flow just above the lava lake must account for.

In any case it is unrealistic to assume that large particles have zero tangential velocity as they leave the surface of the lava lake. We imagine the surface bubbling like a pot of boiling oatmeal. Bubbles burst, releasing hot gas and spattering material in all directions. Some (primarily sulfurous) particles may condense out of vapor in the gas at low altitudes, coupled to the gas, or fine silicate particles may emerge from thin filaments of lava, and these particles will begin their trajectories at the gas velocity or will quickly accelerate to the gas velocity. However, larger particles will only be introduced in the flow via the spattering mechanism, and will often appear with significant tangential velocity (and with some slip in vertical velocity too, relative to the bulk gas).

It is difficult to determine the velocity distribution of dust particles at the lava surface; little is known about particle velocity distributions even for terrestrial volcanoes. Therefore, we examine the sensitivity of the dust velocities at the virtual vent to how they are input at the circular vents on the surface by simulating two cases in which dust particles are initialized with some velocity tangent to Io's surface (Figs. 9b and c). Dust particles enter the domain with a constant speed and a random direction (the velocity vector is

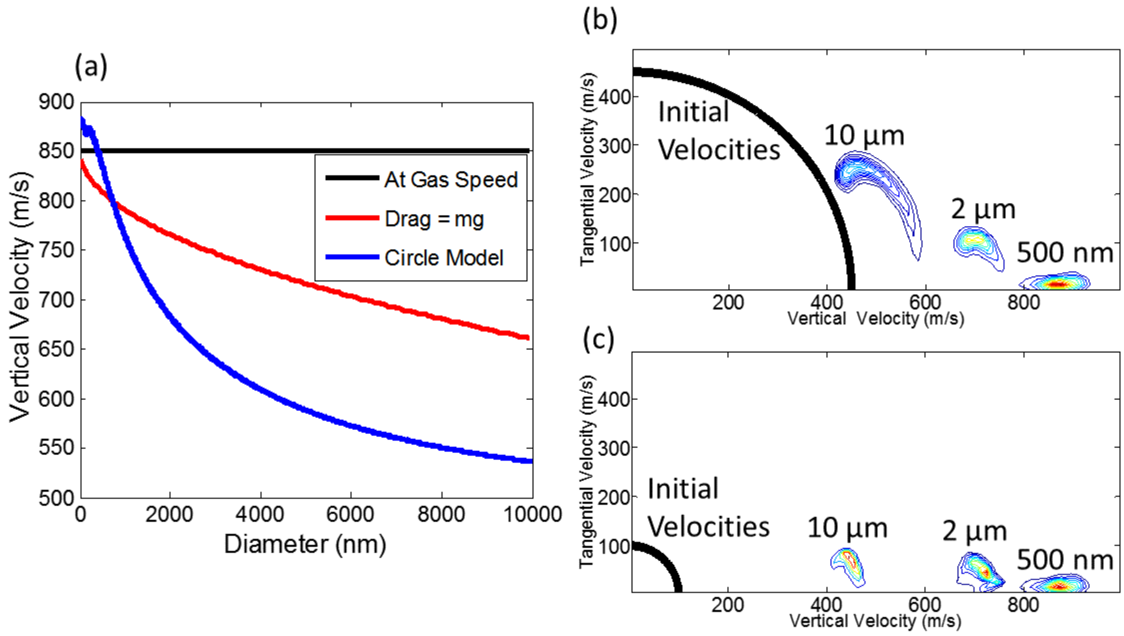

Fig. 9: Dust velocity as a function of particle size at the virtual vent for a variety of possible models. (a) Comparison of vertical velocity at the virtual vent for three "equilibrium" models. The black line shows the gas velocity of 850 m/s at the virtual vent. The red line shows the terminal velocity of dust in the gas at the virtual vent (calculated using an expression for the drag coefficient from Bird, 1994). The blue line shows the average vertical velocity at the virtual vent altitude dust when particles are created at the lava lake surface with 450 m/s vertical velocity and allowed to rise. (b) The 2D velocity distributions at the virtual vent altitude for three sizes of dust when dust is created at 450 m/s oriented in a random direction. The initial velocities of all dust particles lie along the solid black line. (c) The 2D velocity distributions for three sizes of dust when dust is created at 100 m/s oriented in a random direction.

uniformly distributed over the surface of a hemisphere), as appears reasonable for particles being ejected from the surface by bursting bubbles or sprays of lava. This produces large slip velocities between much of the dust and the bulk gas flow in each DSMC cell even very near the surface. Gas flow below the virtual vent remains dense enough to significantly deflect even the largest 10 μm particles used in our simulations, and it will tend to accelerate all dust normal to the surface. However, the bulk gas flow hardly expands laterally below the virtual vent, and at the virtual vent the bulk gas flow is nearly uniformly vertical, so drag will tend to reduce the tangential/horizontal velocity of dust in the flow from the surface up to the virtual vent.

Comparing Figs. 9b and c we see that the velocities of small (< 2 μm) dust particles at the virtual vent are not very sensitive to the choice of input conditions. Whether they are created at an initial speed of 450 m/s (Fig. 9b) or 100 m/s (Fig. 9c), 500 nm particles reach the virtual vent with vertical velocities just over 850 m/s, just as in the zero tangential velocity model in (Fig. 9a), and with a mean tangential velocity of less than 50 m/s. It is clear that such small particles are coupled to the gas at the virtual vent. The vertical velocities of even 10 µm particles are also quite insensitive to the choice of input conditions, and so the large particles will rise ballistically to a characteristic altitude in the plume regardless of their initial speed at the surface. The tangential velocity of large particles is very sensitive to the choice of input condition, however, and tangential velocity affects their deposition patterns, which are discussed in Section 3.2.2, and their line-of-sight integrated column densities (Section 3.2.4). Column density observations allow us to constrain the tangential velocity of large particles at the virtual vent to some extent, but this remains a significant source of uncertainty. For the large plume simulations below, we chose to model the dust as emerging from the circular vents at 450 m/s with a random direction (the case shown in Fig. 9b). These velocity distributions were sampled in order to initialize dust at the virtual vent.

3. Results

3.1. Gas

Computational gas molecules are created in subsurface reservoirs in the source geometry described in Section 2.1 at virtual vent conditions of 500 K, 850 m/s, and 5×10^{18} molecules/m^3 and allowed to expand upwards into four staged domains. The virtual vent altitude is taken to be negligible relative to the canopy height (and the lava lake could be in a depressed area as well). The source geometry causes complicated flow behavior at low altitudes. Flow features that arise near the vent propagate upwards, and sharp gradients can persist even after the flow has become nearly collisionless at higher altitudes below the canopy. During a transient start-up period (Zhang 2004), the simulated plume gas rises much higher than the observed plume canopy. Eventually, under the influence of gravity, the plume falls back on itself, and the canopy shock forms where the weight of the falling gas is supported by rising gas from below. Gas in the canopy is shunted off to the sides of the plume where it forms the large red deposition ring, and the canopy is constantly replenished by new gas rising from the surface such that it becomes a constant feature of the plume.

3.1.1. Near-Vent Flow

The jets of SO_2 rising from the seven source regions (Fig. 2a) exhibit complex three-dimensional structure. In the innermost simulation domains (below 2 km), below the altitude at which the seven sources interact with each other, the geometry of each source region controls the development of the flow in its vicinity. With sources as complex as the ones used here, the resulting flow fields are likewise complex and it can be difficult to predict the flow pattern based on physical intuition. Gas rising from a circular source expands out symmetrically in all directions and becomes less dense as it spreads out and speeds up. With a complex source gas streamlines (lines that follow the bulk velocity of the flow) can converge away from the surface (on the plane between two identical circular sources, for example), and this high pressure region will exhibit higher densities and temperatures. Secondary expansions will occur from these interaction regions. We have previously (McDoniel et al., 2011) illustrated this effect of vent geometry on the structure of the flow at higher altitudes using simpler vent geometries such as a long, curved line. An elongated vent will cause flow far from the vent to expand preferentially perpendicular to the major axis of the vent. A curved source will direct flow preferentially in the direction of its center of curvature.

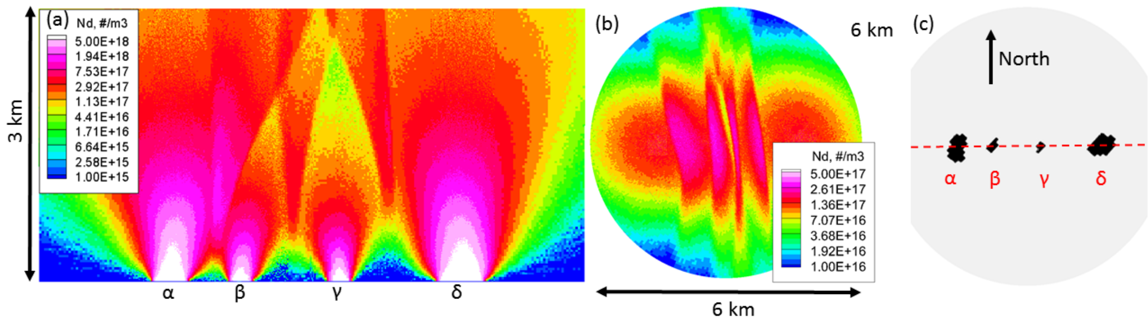

Fig. 10: Number density contours for SO_2 in the immediate vicinity of Source E. (a) A slice of the plume flow seen from the side, along the dashed red line in (c), with gas rising from each of the four collinear vent regions (each is labeled to aid discussion). (b) A constant altitude slice at the top of the domain (3 km altitude). (c) The labeled vent regions, in black, on the same scale as in (b), with a dashed line indicating the orientation of (a).

Fig. 10 shows number density contours just above Source E from our simulated vent. The domain is a cylinder 6 km in diameter and 3 km tall. Interactions between the four source regions produce shocks, and at the top of this small domain the flow approximates flow out of a rectangular slot. Fig. 10a shows how the two smaller regions (β and γ) in the middle emit less gas than the two outer regions, and gas density falls quickly as the flow rises from them. Interactions between the regions produce tall, narrow shocks of high-density gas as fast, low-density expanding gas from neighboring sources meets, slows, and turns. This is a process much like that seen between the circular sources in Section 2.3. The two large outside regions (α and δ) also expand to either side, relatively unaffected by the smaller β and γ regions. Fig. 10b illustrates the preferential expansion of gas away from the major axis of the sources. The two large outer sources are visible as nearly-circular spots on the left and right, and several thin shocks are visible between them. Even though the two smaller central sources are no longer discernible, their presence is partly responsible for the shock structure here. Gas in the shocked regions is expanding much more rapidly to the north and south than it is to the east and west, and this will carry over into later domains. Intuitively, this behavior arises because gas from each of the four sources is continuously flowing outwards in all directions. When the path of the gas is blocked by gas from another source, pressure increases, and the gas is forced out at high speeds in a different direction. Similarly complex flow can be seen just above Sources C and A1 (not pictured). The other four source regions from Fig. 1c (A2, A3, A6, and B1) are simple circles, which produce axisymmetric flow before each interacts with other source regions. Source A1 is the largest, and dominates the later domains, but Source E exhibits many of the same types of flow interactions and is easier to visualize. These flows from different source regions are simulated independently of each other at low altitudes, as with the Source E simulation discussed here, and all seven flows are integrated into a larger domain before they interact with each other.

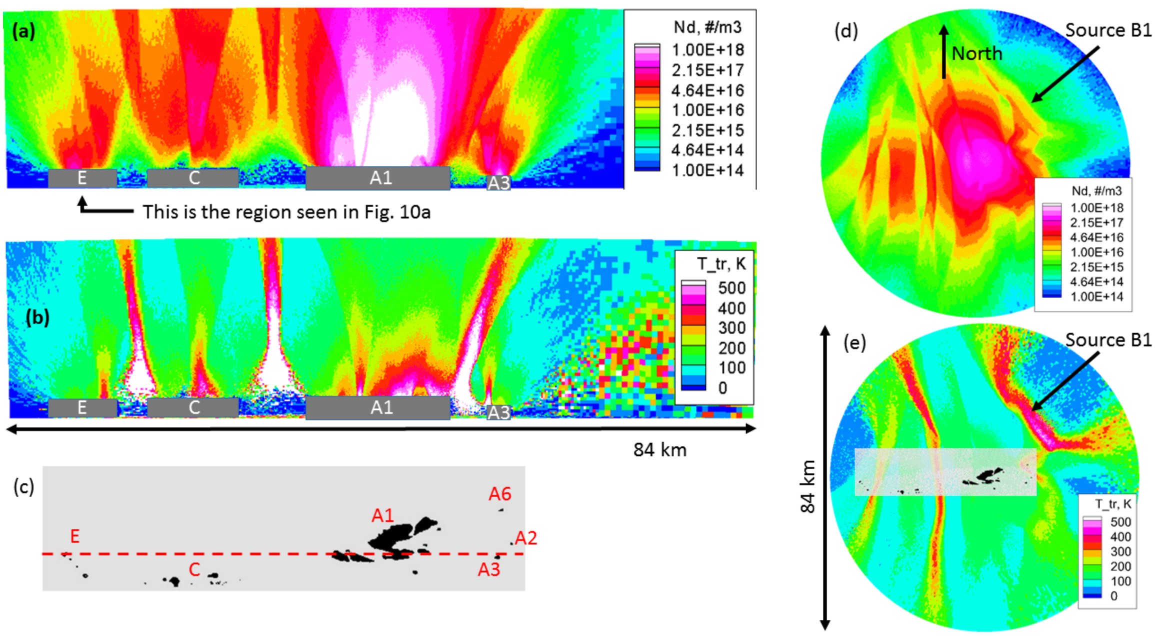

Fig. 11: Number density and translational temperature contours for the first large domain. (a) Number density contours on a slice through the middle of the plume, along the red dashed line shown on the virtual vent in (c). (b) Temperature contours on the same slice as in (a). (d) Number density contours on a constant-altitude slice at the top of the domain (20 km). (e) Temperature contours on the same constant-altitude slice as in (d). The virtual vent is superimposed (Source B1 is not pictured but is labeled).

The seven flows continue to develop in the next domain starting from an altitude of 2-3 km and begin to interact with each other. This domain is 84 km in diameter on the surface of Io and 20 km tall. The same kinds of phenomena seen between the source regions at E occur when flow from Source E meets flow from Source C (or when C meets A1, etc.), and this pattern of converging flow shocking and then expanding out in another direction (generally north and south, given the arrangement of sources) will continue on a larger scale. Fig. 11 illustrates the continued diverging expansion of jets forming from shock regions like those above Source E. In Figs. 11a and b, gas emerges from the individual source domains at the boundaries of the labeled gray rectangles (sections of cylinders in 3D space). Shocks form between the source regions, in much the same way that shocks form between the smaller regions that make up Source E. These shocks interact with each other in complex ways, often merging to form a single, stronger shock extending out at a slightly different angle. High-density gas in shocked regions forms jets which expand outwards at high velocities; one jet emerging from Source A1 is of particular interest for the observable plume flow, and it will later be seen to continue moving to the west, merging with the weaker flows from Sources E and C. The top-down view in Figs. 11d and e show how Source A1 is beginning to dominate the flow, as effects of Sources A2, A3, A6, and B1 are difficult to discern. A region of high density is apparent above Source C. Thin shocks with very high density gradients arise between Sources E and C and between Sources C and A1, as well as within the flow emanating from Source A1 alone. The flow has expanded out more strongly to the north and south than to the east and west, but the highest density is still mostly distributed along an east/west line. Temperature contours (Figs. 11b and e) are useful for visualizing the interactions of the vent regions. The flow is hottest where flows of gas with very different velocities have converged. Rarefaction matters here; the high-temperature area between Source B1 and the other sources is more diffuse than the other high-temperature areas because Source B1 is far away from the other sources relative to its size. The interaction region around it is of lower density than the others and a sharp shock feature cannot form.

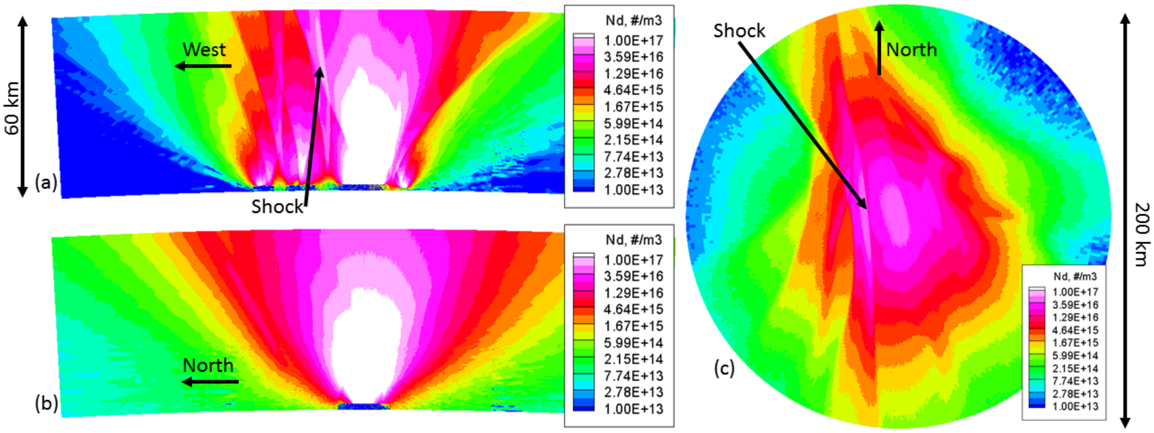

Fig. 12: SO_2 number density contours for the first and second large domains, 200 km in diameter and 60 km tall. (a) Contours for an east/west slice through the plume oriented in the same way as the slice in Fig. 11a. (b) Contours for a north/south slice oriented at 90 degrees to the slice in (a). (c) Contours on a constant-altitude slice at the top of the domain (60 km altitude).

In the penultimate simulation domain (Fig. 12), which is 200 km in diameter and 60 km tall, viscous effects and nearly free molecular expansion smear out some, but not all, of the complexity seen at lower altitudes. The asymmetry of the plume is apparent. In Fig. 12a, the gas continues to expand upwards while preserving many of the features that arose at lower altitudes, whereas in Fig. 12b the plume, viewed from a different angle, might almost be emerging from a circular source (although note that these are thin slices and not line-of-sight integrated column densities). At the top of this 60 km high domain (Fig. 12c), the plume flow appears to contain two dominant features - a large diffuse flow of gas rising out of Source A1 and a sharp, elongated shock centered above Source C. However, this sharp jet is not primarily due to Sources

E and C; it is formed when the strong oblique shock rising out of Source A1 absorbs the flow from Sources E and C. In fact this feature persists even if Sources E and C emit no gas at all; the large-scale structure of the gas plume and the shape of the deposition ring are nearly the same in a simulation of gas emitting from Source A1 only (not presented). By the time gas reaches the top of this domain, there are few collisions occurring, and the residual asymmetry of the flow will persist into the final domain. It is important for the deposition patterns that an axis-switch has occurred; the major axis of the gas flow at this altitude is roughly north/south, whereas at lower altitudes, especially immediately above the virtual vent, the bulk of the gas is located near an east/west line. The gas will continue to expand out preferentially along this north/south axis, explaining the north/south elongation of Pele's red ring.

3.1.2. Gas Canopy and Column Density

Gas in the final domain, which is 1,600 km in diameter and 440 km tall, expands in a nearly free-molecular fashion until it reaches the canopy shock. Knudsen numbers based on the canopy height or on the length scale of density gradients remain small (O(10^{-3})) on the plume's centerline just below the canopy, indicating that collisions are somewhat important, but the mean free path is hundreds of meters and temperatures are low. Note that the mean free path is measured in a reference frame moving with the bulk gas; just below the canopy, molecules only collide once for every 1-2 km they travel upwards, on average, because of the flow's large upwards bulk velocity. Gravity is by far the most important influence on the gas just below the canopy. Early in the simulations, before the canopy shock forms, the gas continues to an altitude of $\sim$500 km before falling back down. This falling gas collides with still-rising gas and causes the development of the canopy shock. Thereafter, rising gas sustains the canopy shock and replenishes gas above it as canopy gas flows around the sides of the plume to the ground, forming the deposition ring.

The plume flow in this final domain is notable for its continued asymmetry. Longitudinal slices of the plume taken at different angles are different from each other. Fig. 13c shows a north/south slice of the plume, nearly through the major axis of the deposition ring. At this angle, the plume appears regular and might be mistaken for the output of a large, round hole. The rising gas supports a round canopy that curves over the plume until it intersects the surface. However, in Fig. 13a, several irregular flow features are apparent. The oblique shock seen at lower altitudes continues merging with expanding jets from Sources E and C and gives rise to a high-density finger of gas which displaces the canopy shock by about 25 km. The canopy is also much less developed at this angle and becomes less dense more quickly as the gas falls around the sides of the plume to the ground. This is due to the axis-switching behavior pointed out at lower altitudes (Section 3.1.1); less gas expands out along the east/west axis. The canopy intersects the ground closer to the plume's source as well, and this will be seen clearly in the simulated deposition pattern.

Number density along the plume's centerline falls to about 1.6×10^{15} m^{-3}, which is lower than the density at the virtual vent by a factor of almost 4,000 (and lower than the density at the lava lake by a factor of

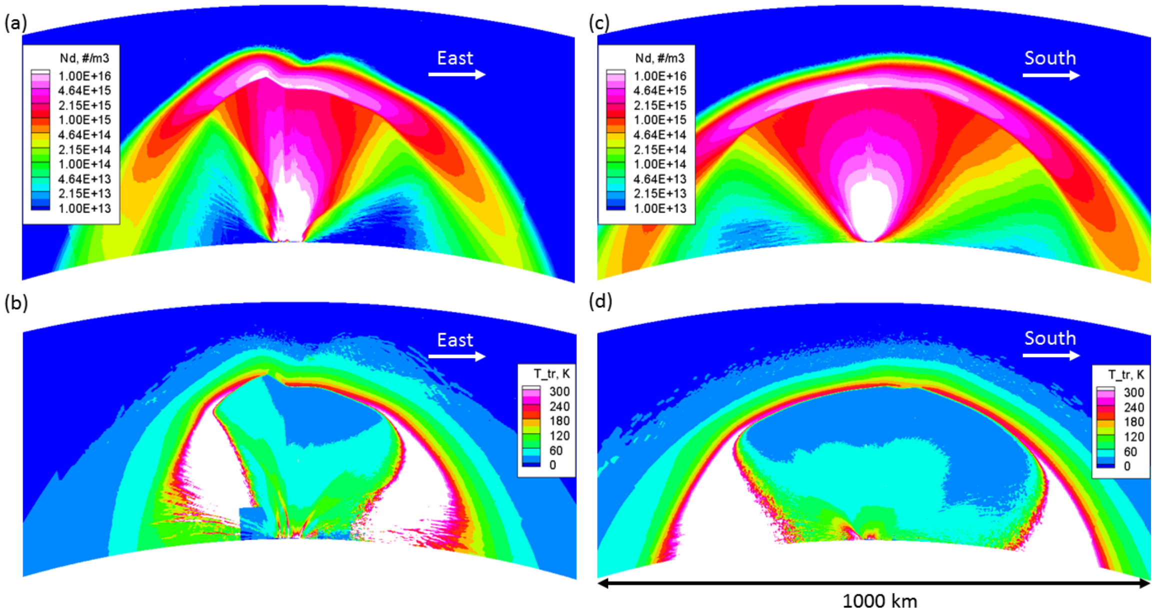

Fig. 13: SO_2 number density and temperature contours for all three large domains, 1,600 km in diameter along the surface of Io and 440 km tall. (a) Number density contours on an east/west slice showing the continued expansion of the smooth flow in Fig. 12. (b) Translational temperature contours for the slice in (a). (c) Number density contours on a north/south slice. (d) Translational temperature contours for the slice in (c).

about 1.6×10^5), before shocking back up to about 10^{16} m^{-3}. This may appear to be a surprisingly weak expansion (the flow is only about Mach 8 just below the canopy shock), but on this scale gravity plays a large role and removes a great deal of energy from the gas (roughly half of the kinetic energy in the gas at the vent has been lost by 350 km altitude). Peak centerline vertical velocity (of about 1,000 m/s) was actually reached at around 50 km altitude. Gravity outpaces continued expansion above this altitude. Figs. 13b and d show the gas cooling as it expands upwards before heating in the canopy after it shocks. High-temperature regions closer to the vent were used as markers for the interaction of source regions. Here, the extremely "hot" regions inside the canopy to either side of the vent indicate where the flow is highly non-equilibrium (Zhang et al., 2003). Because densities in these regions are so low and collisions are so rare, gas falling from the canopy passes through gas expanding outwards and upwards directly from the vent. The resulting velocity distribution is non-Maxwellian, effectively being two non-interacting streams of gas, and so the computed kinetic temperature (which is by definition the root mean square deviation of molecular velocities from the mean gas velocity) must be interpreted with caution. The cold artifact seen just to the left of the source in Fig. 13b illustrates the one-way coupling between the domains; this is the temperature of only the expanding gas in the penultimate domain, unaffected by gas falling from the canopy in the final domain.

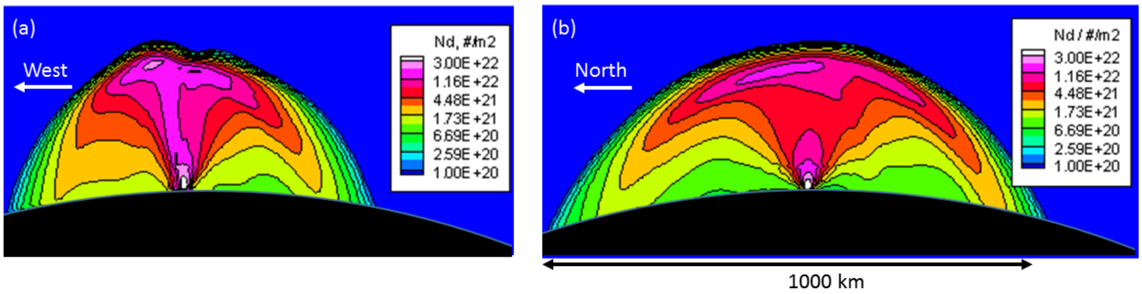

Fig. 14: SO_2 line-of-sight integrated column densities. (a) Column density seen from due south. (b) Column density seen from due west.

Remote observations of plumes visualize line-of-sight columns of particles rather than slices, and one might suspect that integration in space would smear out much of the asymmetry described above. However, this is not the case, and simulated north/south column densities look quite different than simulated east/west column densities (Fig. 14). The strong oblique shock feature is less visible (though still apparent in Fig. 14a) in an integrated image, but the three-dimensional nature of the canopy shock is clearly evident, and the kink in the canopy seen in Fig. 13a is still visible. Unsurprisingly, the regular slice of Fig. 13c predicts the regular column density of Fig. 14b; here the plume appears similar to axisymmetric plume simulations (Zhang et al., 2003), with smooth expansion to a relatively uniform canopy. That such asymmetry is possible suggests that it will be difficult to draw conclusions about the structure of plumes from observations taken from only one angle. Very fine particles in the plume which remain fully entrained in the gas flow will exhibit similar line-of-sight column densities. Condensate, which may preferentially form/grow in the canopy, should exhibit these asymmetries. Heavier dust, however, will decouple from the gas flow and may behave differently, so further simulations are required to explain observations of large particles (Section 3.2.4).

3.1.3. Gas Deposition

In our simulations, gas from the canopy falls to the ground in a narrow band, creating a ring of intense gas deposition. As discussed earlier, if we assume that the observed red ring is the result of deposition of S_2 or other molecules or particles that track the gas, then the simulated gas deposition can be directly compared to the observed red ring, at least in a qualitative sense. Simulated deposition images are also a useful way of visualizing the three-dimensional canopy, since the ring appears where the canopy intersects the surface and the simulated deposition rate (mass flux to the surface) is roughly proportional to the canopy density at the surface (it varies somewhat depending on the downward velocity in the canopy at the surface, but this is nearly constant all around the ring). Our simulated deposition patterns are obtained by recording all particles that impact the surface over a period of 1,000 seconds once the plume has reached a steady state (i.e. with a stable canopy shock and instantaneous deposition rates that only vary with statistical noise).

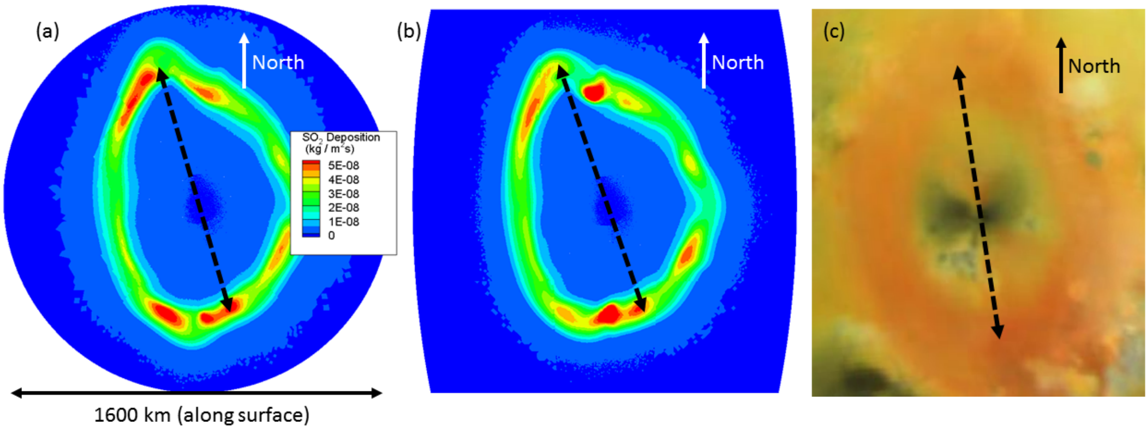

Fig. 15: Gas deposition patterns. (a) Contours of the deposition rate of SO_2 on the surface (in kg / m^2s) for the plume simulations. (b) Contours of the deposition rate of SO_2 when we implement fictitious forces to account for our non-inertial reference frame. The plume shown here was simulated at the equator of Io. (c) Pele's ring on Io's surface, as seen from the same head-on perspective used for the simulations, drawn from Williams et al. (2011). Lines of maximum diameter are drawn on all images.

The simulated deposition ring (Figs. 15a and b) is egg-shaped, with a larger diameter, higher deposition rate, and increased ring thickness to the north and south of the vent than to the east and west, as suggested by the slices shown earlier. It is sharper in the north and south, with particularly intense deposition at these ends. The peak deposition rate is roughly 7.5×10^{-8} kg/m^2s, and in every direction from the vent there is some area where deposition is more intense than 2×10^{-8} kg/m^2s. The effect of Io's rotation and revolution about Jupiter causes a change in the ring's orientation, albeit a small one of just a few degrees. Fig. 15a shows the plume in a domain 1,600 km across centered at the north pole, while Fig. 15b shows the same plume centered at a point on the equator, with fictitious forces included to account for Io's rotation and revolution about Jupiter.

The shape and orientation of the simulated ring are in good qualitative agreement with observation. Direct comparisons are difficult to make because, on this scale, the curvature of Io is important. Lacking an observation from directly overhead, a simulated image from directly overhead can be compared to a composite of observations such as the global map of Williams et al. (2011), as in Fig. 15c. This image was obtained by wrapping the Williams et al. map around a sphere and orienting it such that Pele's source is the closest point to the viewer and a vertical line down the center of the image corresponds to a line of constant longitude - it is an azimuthal orthographic projection centered on Pele. With this adjusted perspective, we can compare the simulated (a) and observed (c) deposition patterns quantitatively, although this comparison will still be inexact due to the diffuse nature of the plume's deposition pattern. We choose points in the ring due north, south, east, and west of the source, as well as at the ends of the longest diameter. The simulated ring is ∼8% wider than the observation from east to west. It is ∼4% too long north to south. It is ∼3% too long along its maximum diameter, which is ∼1,000 km (this is a projected distance that does not account for the curvature of the moon). We can also compare the angle between due north and the maximum diameter. In the observation we find that this angle is ∼15 degrees; in our simulation this angle is ∼14 degrees. The orientation of the simulated ring is almost exact, and several measures of ring size are very close.

These simulations do not include a background atmosphere, planetary winds, or interaction with Jupiter's plasma torus. The excellent agreement between the simulations presented here and observations suggests that these excluded phenomena are unimportant to the deposition process. This might be because deposition occurs mostly at night when the background atmosphere is negligible, while plasma is absorbed in the canopy, inflating an upper layer but not strongly affecting the bulk of the gas flow to the ground. These issues will be addressed in a subsequent paper.

Fans of orange/red deposition are visible to the north and south of the vent in observations. While there is some deposition in similar locations in the simulations, and more than there is to the east and west of the vent, it is not nearly as intense as the ring deposition. This difference could be due to several factors. The observed ring deposition may be saturated, edge-of-the-lava-lake effects below the virtual vent may be important for explaining gas depositing near the vent (see Section 2.3), or the canopy may shield the inside of the ring from overlaying deposition by atmospheric gas. Pele's deposition ring is also not constant over time (Geissler et al., 2004), and our simulations cannot capture this long-term variability, although some simulations (not presented) suggest that unsteadiness due to instability in the flow is possible even with a steady source. Some preliminary results suggest that small fluctuations at the vent or in the canopy can cause a transient buckling inward of the southern edge of the ring as seen in the survey of surface changes by Geissler et al., but this requires further study. We also see suggestive jets of gas to the north and south of the lava lake in constant-altitude slices just above the surface of Io (related to the north/south expansion in Fig. 12c), which correspond well to the red fans to the north and south of the lava lake in observations. Anything that disturbs these jets might produce deposition where the red fans are observed (see Section 4.1).

3.2. Dust

Dust particles of sizes between 20 nm and 10 µm are created in the flow at the virtual vent with velocities chosen according to the function determined in Section 2.4. Their real number density is assumed to be arbitrarily small so that they do not affect the gas flow. Dust particles have a density of 800 kg/m^3, which is a little on the low side, but which is intended to partially account for the difference between real grain geometries and the simulated spherical particles. Irregularly-shaped real grains will have larger aerodynamic cross-sections than spherical particles of the same mass.

3.2.1. Dust Flow by Size

Even though dust particles in the real plume will exhibit a wide distribution of diameters (and shapes and compositions) spanning the entire range from 20 nm to 10 μm, simulations of a set of narrow distributions are useful for understanding how the particle diameter affects its motion through the plume. All distributions shown in this subsection are uniform, taking on all integer nanometer values in their range (e.g. for a 20-24 nm distribution, 20% of the particles will be 20 nm, 20% of the particles will be 21 nm, etc.).

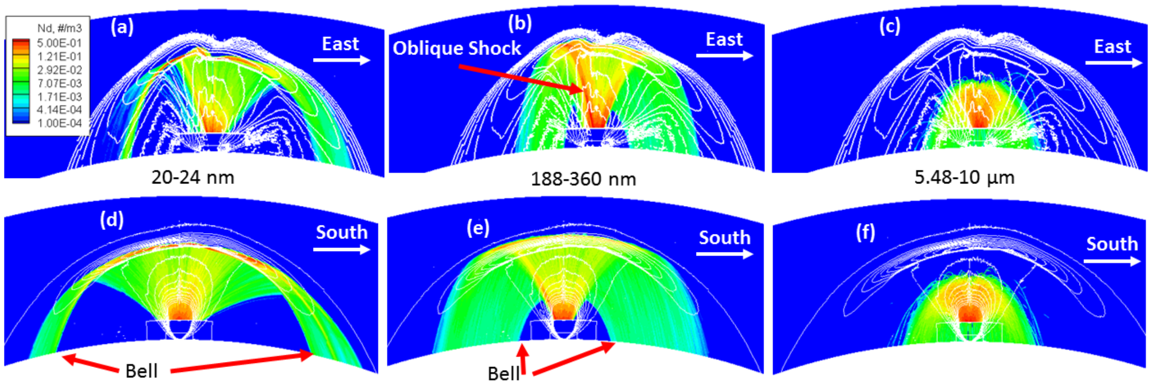

Fig. 16: Number density contours for several narrow size distributions of dust grains, with superimposed line contours of the gas slices from Fig. 13. (a), (b), and (c) show slices for three distributions seen looking north, while (d), (e), and (f) show slices for the same size distributions seen looking east. Only flow in the final simulation domain is shown and the absolute value of the number density is arbitrary due to our low mass loading assumption, but relative magnitudes are valid.

While very small dust particles (∼1 nm diameter) should track the gas flow, larger particles tend to exhibit trajectories characterized by largely ballistic motion subject to a small drag force from the bulk gas flow which acts to nudge the dust in the direction of the gas flow. Dust of up to about 1 μm is strongly coupled to the gas at the virtual vent and sizes up to several microns are weakly coupled (Section 2.4), and all simulated sizes decouple from the gas flow to some extent as altitude increases (and gas density falls). This results in dust particles encoding information from the gas flow at low altitudes, preserving low-altitude features of the gas flow better than the gas itself does, with the degree of preservation depending on particle size.

Fig. 16 shows plume slices for some sample particle size distributions. Asymmetry is obvious for the two smaller size distributions, but not for the largest. Particles from the smaller distributions reach a maximum altitude at approximately the canopy height, whereas particles from the largest distribution, having decoupled near the virtual vent, travel ballistically to a much lower maximum altitude. Smaller particles, which remain coupled to the gas flow, are dragged upwards by expanding gas, attaining higher maximum altitudes. However, the maximum altitude of the dust in (b) and (e) is actually slightly higher than that for the lighter dust in (a) and (d). The smallest particles adjust to the gas quickly, and stop rising soon after encountering stationary gas in the canopy. Somewhat larger particles, while still partially coupled to the gas, rise through the stationary canopy for some time before drag and gravity bring them to a halt. The largest particles (Figs. 16c and 16f) do not even reach the canopy before beginning to fall back to the surface.

The small particles in Figs. 16a and 16d are nearly fully-entrained in the gas flow. Flow features in the dust correspond well to those in the gas, even tracking the canopy all the way down to the surface. The larger particles in Figs. 16b and 16e have decoupled to some extent before reaching the canopy. The oblique shock feature seen in Fig. 13a is much more apparent in Fig. 16b, because the partially decoupled dust preserves this sharp feature from lower domains (Fig. 12a) better than the gas does. These particles are also too large to be entrained in the canopy, and they fall out of the canopy close to the central axis of the plume, impacting the surface much closer to the lava lake than does the gas. However, particles do not move ballistically as they travel back down through the plume. As seen in Fig. 16e, a bell forms around the source of the plume where dust does not reach the surface (this phenomenon in axisymmetric plumes was reported in Zhang et al., 2004). This is due to falling dust being deflected to the sides by rising gas. This deflection is also visible in Fig. 16d, but in Fig. 16f the particles are so large that the gas does not prevent them from falling straight down into the inner domains (the influence of rising gas in the inner domains on this dust is not simulated). The largest particles (Figs. 16c and 16f) also decouple from the gas flow before asymmetry develops on a large scale and so they preserve information from below the virtual vent. The trajectories of these particles are therefore most sensitive to the choice of dust input condition from Section 2.4 and are almost totally insensitive to developments in the gas flow above the virtual vent.

3.2.2. Dust Deposition by Size

An important result of the tendency of dust to preserve gas flow features from low altitudes is that dust does not exhibit axis-switching behavior to the same extent as the gas, except for the smallest particles. Relatively more dust is directed to the east and west of the lava lake, and this can produce deposition patterns that look nothing like the deposition ring left by the gas. These deposition patterns, like the dust density contours from Section 3.2.1, are strong functions of particle size; we see a transformation from patterns that resemble the gas ring for very small particles, through stripes to the east and west of the lava lake for medium sizes, and finally to roughly axially-symmetric bullseyes on the surface for the largest particles.

Fig. 17 shows the deposition patterns produced by five different size distributions of dust particles which are uniformly distributed in the gas flow at the virtual vent. The smallest particles (Fig. 17b) reach the surface in a thin ring with features corresponding to those of the gas ring. This supports the conclusion from Section 3.2.1 that these small particles remain coupled to the gas flow throughout the entire plume.

As particle sizes increase, dust deposits more densely in a smaller area. The slightly larger dust in Fig.

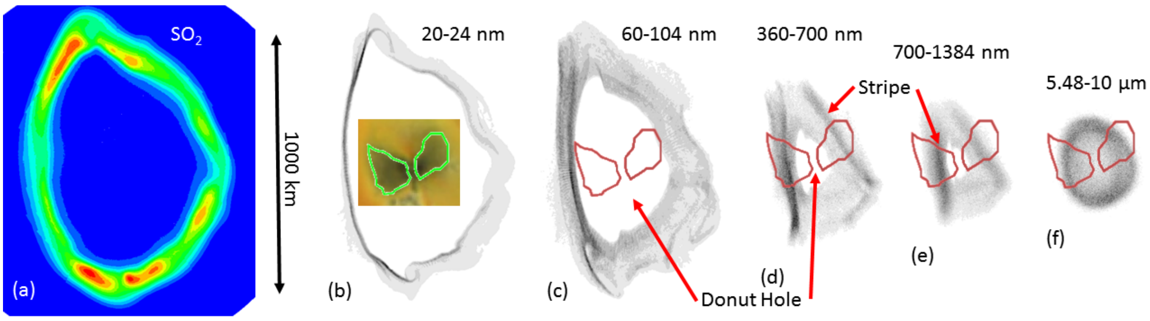

Fig. 17: Simulated deposition patterns for various sizes of dust grains, with the gas deposition ring for scale in (a). Pixel darkness is proportional to deposition rate and is normalized by the total number of simulated particles of each diameter. The target region and observation are shown on (b) and the target region is outlined on the other simulated dust deposition patterns.

17c still falls to the surface in a ring which resembles the gas ring, but many particles are falling out of the canopy before reaching the surface. However, there is still no dust deposition at all in some region surrounding the lava lake (for all but the largest size distribution). These "donut holes" correspond to the bell shapes seen in the dust flow in Fig. 16; falling dust that was initially entrained in the gas flow at the virtual vent cannot impact the surface in these donut hole regions because of deflection by rising gas.

In Fig. 17d, the particles deposit in a much smaller pattern than seen in Figs. 17b and c. Rather than forming a clear ring shape, these particles primarily fall in two long stripes to the east and west of the lava lake, with light deposition between them (except for in the "donut hole"). The stripes form because these particles decouple at low altitudes in the plume such that they preserve low-altitude gas features (Section 3.2.1). These medium-size particles are initially swept along by the gas into the shock structures seen in Section 3.1, but then decouple and are not dispersed along with the gas as the gas continues to expand. These concentrated sheets of dust particles continue on nearly ballistic trajectories until they form stripes on the surface. This feature is seen in the dust flow in Fig. 16b. As particle size continues to increase, as in Fig. 17e, this distinctive deposition pattern continues to shrink in size.

The largest particles (Fig. 17f) fall to the ground in a roughly symmetric spot or bullseye pattern. This is due to the early decoupling of large particles, which are not swept into the gas shocks in the first place, and corresponds to the nearly symmetric dust trajectories in Figs. 16c and f. Deposition is somewhat more intense in a ring around the outside of the spot, which is largely an artifact of the initial velocity distribution chosen for the particles (Section 2.4). It is possible that a distinct donut hole would be seen even for the largest dust particles if deflection from rising gas in the inner domains (through which these large particles fall) were simulated.

3.2.3. Best-Fit Dust Size Distribution

As described in Section 2.2, we can obtain a best-fit size distribution by simulating a series of dust size distributions like those in Sections 3.2.1 and 3.2.2 and finding the linear combination of their deposition patterns which best matches the observed region (from Fig. 3). Recall that we intend to compare to a target region consisting of the "butterfly wing" regions to the east and west of the lava lake (Fig. 3d), excluding the immediate vicinity of the lake (so potential error due to a lack of a "donut hole" for the largest size distributions is irrelevant). With the results from Fig. 17 in hand, we observe that our fitting method will be unable to constrain the relative amount of the smallest particles in the plume, because these particles fall to the surface directly on top of the gas deposition ring (which is outside of our target region, and in which red sulfur deposition would overlay the dust). Last, we note that the stripes seen in Figs. 17d and e are promising; they produce the most intense deposition in the "butterfly wings" and relatively little deposition in the excluded regions. Because the stripes move closer to the lava lake as particle size increases, one can imagine how a wide range of particle sizes might produce black fans to the east and west (the superposition of several stripes) with relatively little deposition elsewhere.

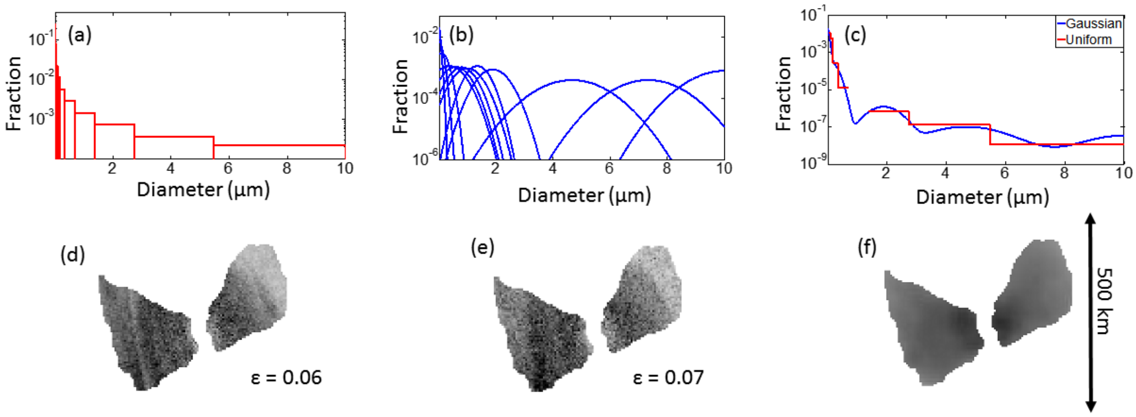

Fig. 18: (a) Set of uniform basis function size distributions. (b) Set of Gaussian basis function size distributions. Basis functions are normalized such that the sum of the values a basis function takes at all integer nanometer diameters between 20 nm and 10 μm is 1. (c) Best-fit size distributions obtained using the basis functions in (a) and (b). (d) Best-fit deposition pattern in target region obtained from the basis functions in (a), which is produced by the best-fit distribution in red in (c). (e) Best-fit deposition pattern in target region obtained from the basis functions in (b), which is produced by the best-fit distribution in blue in (c). (f) Target region from observation. Note the log scales on (a), (b), and (c), and in all cases "Fraction" represents the number fraction of particles in a distribution at each integer nanometer diameter.

The choice of what form to use for the simulated size distribution basis functions, how many of them to simulate, and what paramaters to use for the individual distributions, is somewhat arbitrary. We performed simulations for about 30 basis functions, some uniform (like those presented above) and some Gaussian, as we explored various ways of spanning the space of grain sizes from 20 nm to 10 μm. We chose to use narrower distributions at smaller mean particle sizes because instantaneous acceleration due to drag is inversely proportional to particle size, because a particle's contribution to deposition is proportional to the square of particle size, and because we wanted to be able to represent an approximately log-normal best-fit distribution. As seen in Fig. 17, size distributions which broaden as particle diameter increases produce deposition patterns with features of roughly uniform width. We typically used 9-12 basis functions when producing a best-fit size distribution.

Fig. 18 shows the best-fit deposition patterns and size distributions produced by two different sets of basis functions. Fig. 18a shows a set of 12 non-overlapping uniform ("top hat") basis functions, which produce the best-fit deposition pattern in Fig. 18d within the target region. Fig. 18b shows a set of 12 Gaussian basis functions, often with significant overlap, which produce the best-fit deposition pattern in Fig. 18e. Errors in the fit are small; the sum of squared residuals divided by the sum of the squared target data is about 7% for both. The best-fit size distributions obtained by applying the least squares coefficients to the basis functions directly are shown in Fig. 18c. The two best-fit distributions are close, suggesting that the form of the basis functions and their degree of overlap are unimportant. Both drop significantly around 1 µm, with the uniform basis functions yielding no particles at all between 700 and 1,384 nm (this is the basis function whose deposition is shown in Fig. 17e). The Gaussian basis functions also yield no contribution from size distributions with means in that range, but we find particles at 1 µm anyway due to the long tails on these functions. This drop persists in the best-fit size distributions for many other sets of basis functions, including sets that contain several very narrow distributions centered at 1 µm.

The best-fit size distributions we obtain decrease by about six orders of magnitude as particle size increases. Surface darkness varies by less than an order of magnitude over the target region, and in our model particles darken the surface in proportion to their number fraction, so the fitting process is relatively insensitive to exactly how dark the surface is. If regions close to the lava lake where only large particles fall were ten times darker, there would only be about ten times as many large particles in the best-fit size distribution, so that the best-fit size distribution would decrease by about five orders of magnitude from 20 nm to 10 µm. Likewise, fitting to a uniformly dark surface inside the butterfly wings produces a result much like the one obtained here. The steady decrease in the best-fit distribution with particle size is due mostly to our darkness model (Section 2.2) and to the importance of particle size for explaining how far from the lava lake particles travel before they deposit (Fig. 17). In our model, particles darken the surface in proportion to their cross-sectional area, so even if 10 µm particles are responsible for as much surface darkening as 100 nm particles, there will still be fewer of them by a factor of 10^4. As seen in Section 3.2.2, as particle size increases from 20 nm, the distance from the vent at which particles deposit shrinks, rapidly at first, then more slowly. Larger particles (which fall closer to the vent) will tend to deposit with higher densities than smaller particles just because they are falling in a smaller area. We also observed earlier (Fig. 17) that increasing the width of basis functions as particle sizes increase produces deposition patterns with roughly uniformly wide features. This effect tends to yield more small particles in the best-fit distribution; because particles from 700-1,384 nm fall to the ground in an area about as wide as the area in which 60-104 nm particles fall, fewer particles at each diameter between 700-1,384 nm are necessary to coat the surface with some density of particles. That is, the deposition patterns become more "tightly packed" as particle size increases, and this decreases the number of particles of any particular diameter which are necessary to explain a given surface coloration. It should also be noted that there are other ways to represent the best-fit particle distribution, for example as a distribution of the fraction of particles with some cross-sectional area, or as a fraction of the total mass of the dust at each diameter. The cross-sectional area or the mass distributions can be obtained from our result by biasing the fraction by d^2 or d^3, and so they are much flatter.

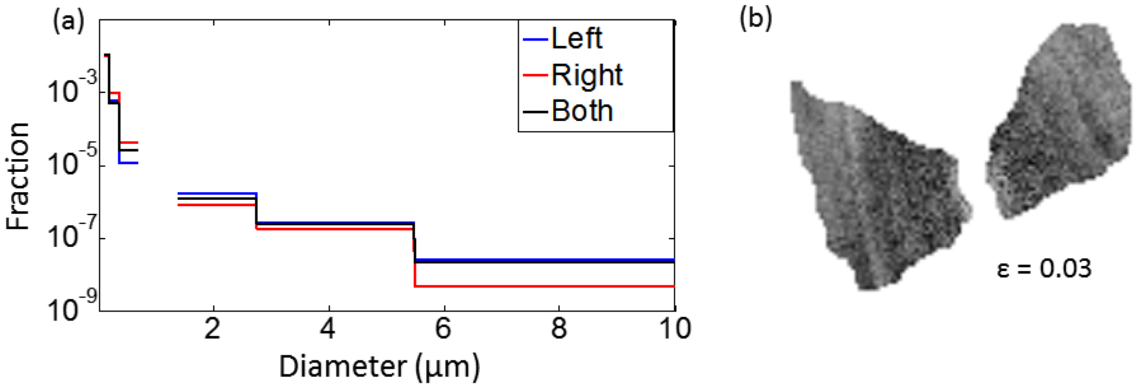

Fig. 19: (a) Comparison of the best-fit size distribution obtained earlier (Both) to those obtained when each butterfly wing is fit independently (Left and Right). (b) The composite best-fit deposition pattern produced when fitting each wing independently. The uniform basis functions from Fig. 18a were used.

An important source of fitting error is that our best-fit deposition patterns are consistently too dark in the western butterfly wing and too light in the eastern wing compared to the observation. The two wings can be fit separately, yielding two new best-fit size distributions (one for each wing). The composite best-fit deposition pattern (Fig. 19b) is a closer match to the observation. It is darker on the eastern edge of the east wing, and error has fallen to 3%. This is unsurprising, since this approach allows more degrees of freedom when fitting. However, Fig. 19a compares the best-fit size distributions obtained by fitting just the left wing, just the right wing, and both simultaneously, and all are remarkably similar. All of the distributions are within a factor of 3 everywhere except in the range of the largest basis function, where they differ by a factor of ~10. However, the eastern wing is relatively uninfluenced by this basis function's deposition, so this is not an important distinction. Note that the eastern wing must play almost no role in determining the fitting coefficient for this basis function when both wings are fit simultaneously, since the other two best-fit distributions are right on top of each other in this range. The important source of error in the simultaneous fit is in the basis functions between 188-360 nm and between 360-700 nm. In fact, the deposition patterns for individual basis functions in Fig. 17 show a tendency to produce more intense deposition to the west of the lava lake than to the east, and this tendency is strongest for smaller particles. The possibility that this error is due to a failure to account for differences in the characteristics of the simulated source regions is discussed in Section 4.2.

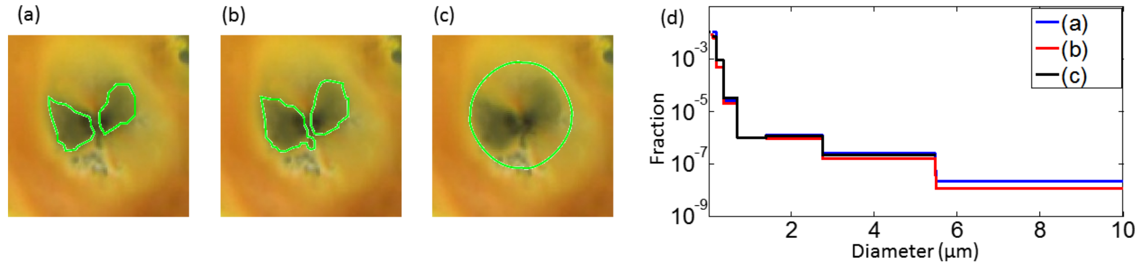

Fig. 20: (a) The target region used earlier. (b) A more generous target region which tries to capture nearly everything that could plausibly be due almost solely to dust deposition. (c) A circular target region extending out to the inner edge of Pele's red ring. (d) A comparison of best-fit size distributions obtained for different choices of target region.

The choice of target region has some effect on the best-fit size distribution, but only a small one. The target region was chosen so as to include only areas where the coloration of Io's surface seemed likely to be dominated by the rate at which dust deposited on the surface (e.g. not part of the large red ring and not north and south of the vent where gas deposition is important) and where the simulation is thought to be reliable (e.g. not in the immediate vicinity of the vent, in part due to the error discussed above in the deposition of the heaviest dust falling back into the inner domains). Performing the same calculation with a variety of different target regions produces very similar best-fit size distributions (Fig. 20), although the large circular region of Fig. 20c yields a contribution from elusive 1 μm dust. The fitting error increases significantly, but this is to be expected if our initial assumption that dust deposition alone cannot explain the surface coloration outside of the target region is a good one. The error increases because the simulated dust deposition cannot explain coloration due to the deposition of other materials which fall to the ground in qualitatively different patterns outside of the original target region.

3.2.4. Dust Column Densities

Line-of-sight integrated column densities of dust particles in the plume provide another opportunity to compare simulation and observation. It is difficult to make as direct of a comparison as in the previous section because observations are more limited and because observations do not distinguish between ash particles and condensate. Nonetheless, there is insight to be gained.

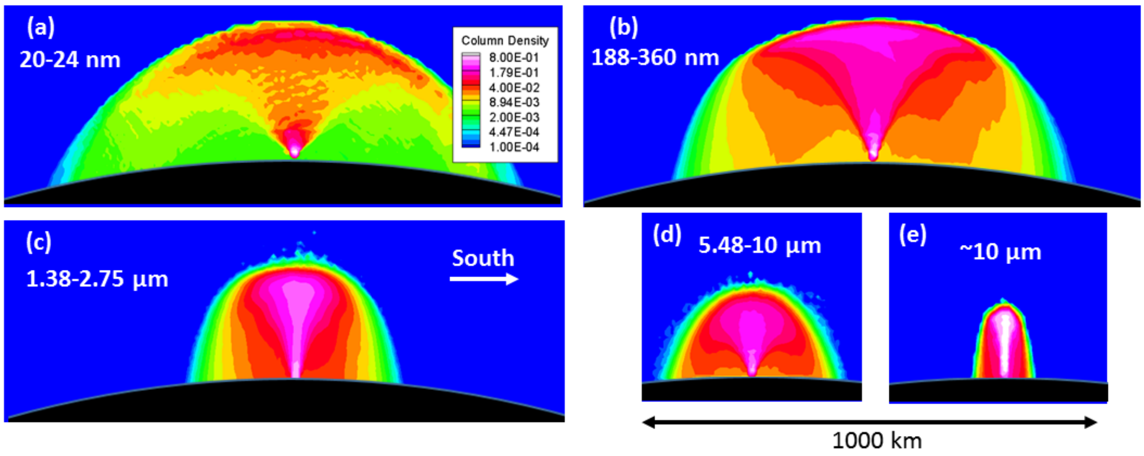

Fig. 21: Normalized line-of-sight integrated column densities for several size distributions of dust. (a), (b), (c), and (d) are uniform size distributions similar to those used in previous figures. (e) shows column density for the largest Gaussian basis function from Fig. 18b, where the dust is created at the virtual vent with a velocity of 450 m/s directly upwards, and no velocity parallel to Io's surface. All images are shown looking east.

Fig. 21 compares line-of-sight integrated column density for several kinds of particles. In Fig. 21a, the lightest particles produce column densities like the SO_2 column density in Fig. 14b. As particle size increases, column densities in the core of the plume increase and the visible canopy shock becomes limited to the central axis of the plume before eventually disappearing, in line with what was seen for slices of particles in the plume in Fig. 16. Figs. 21d and e compare two different input conditions for dust at the virtual vent. Fig. 21d shows the heavy dust used in results elsewhere in this paper, with a velocity distribution obtained from the sub- virtual vent model where the particles are given initial velocities of 450 m/s oriented in a random direction. Fig. 21e shows pencil-beam column densities which are produced by heavy dust initialized at the virtual vent with no velocity parallel to Io's surface. Even if there are relatively few large particles in the plume, the column density of large particles (created with no tangential velocity, as in Fig. 21e) at 150 km altitude remains nearly as high as it is at the virtual vent, because these particles remain in a tight column instead of spreading out. In spatially-resolved observations, this feature should be visible far out of proportion to the number of large particles in the plume as a whole if large particles are actually entrained in the gas at the virtual vent altitude. However, no such thin column feature is observed (Fig. 22).

Because the three-dimensional Pele plume looks so regular from this angle, these results can be compared directly to column densities for particles simulated by Zhang et al. (2004). The results here are rather similar, except that the 20-24 nm particles correspond well with the 1 nm particles in Zhang et al., and likewise the 188-360 nm particles here most closely resemble the 10 nm particles in Zhang et al. The difference is largely due to vent geometry. Even though the plumes simulated in both works have the same mass flow rate, the vent used here is about an order of magnitude smaller in total area than the one used by Zhang et al. (who used a circular hole 8 km in radius). Gas densities just above our virtual vent are therefore an order of magnitude higher and particles are more strongly influenced by the gas as it initially expands upwards. This imparts higher velocities to particles before they decouple from the gas.

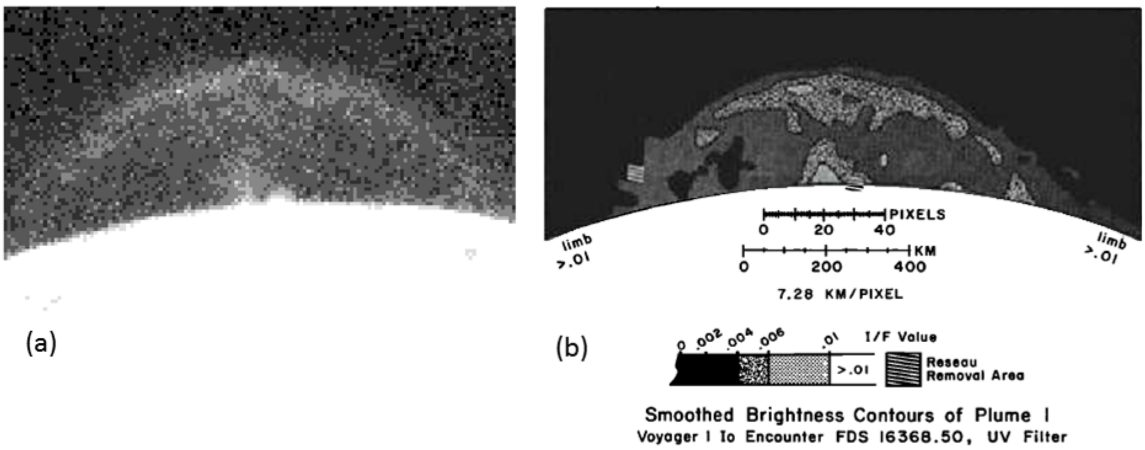

Fig. 22: (a) Voyager 1 observation of Pele through its UV filter. Image from PDS C1636850, stretched and saturated to better show the plume. (b) Contour levels for the observation in (a) from Strom et al., 1981.

We can also compare these results to a Voyager 1 observation of Pele in the UV (Fig. 22). While it is possible to construct a "best-fit column density" from our best-fit size distributions by using the fitting coefficients determined in Section 3.2.3 and weighting the contributions of each particle size by its coefficient α_k and by a scattering cross-section, heavier particles dominate and the result does not resemble observation (keeping in mind that the fitting method used could not constrain the smallest particle sizes due to their deposition patterns overlaying the gas ring). The column densities for 20-24 nm particles shown in Fig. 21a is the closest match to the observation and contours in Fig. 22. The column density of the smallest dust particles features a distinct canopy as well as a high-density region close to the surface, corresponding well with these features in Fig. 22b. Small particles in these simulations more closely resemble the observation than did the small particles in Zhang et al., 2004, which formed a pencil-beam structure near the surface (due to the larger vent area and slower expansion). This led Zhang et al. to suggest that large particles would be necessary to fit the near-surface feature in the observation, but that does not appear to be the case with our simulations. Further, the number of small ($<\sim$60 nm) particles in the plume is unconstrained by our simulations, both because small particle deposition was coincident with the gas ring and because our simulations do not include SO_2 condensate, so it is possible that very large numbers of such particles are present. Very large particles are also unconstrained by our simulations due to the choice of target region on the surface, if they are slow enough at the virtual vent to remain in the lava lake's immediate vicinity. Such particles would also not rise very high and so would be unconstrained by observed column densities.

4. Discussion

4.1. Gas Modeling

The remarkable agreement between the simulated and observed gas deposition ring strongly suggests that the plume model which produces that simulated ring is essentially correct. However, there are two features of observations of the gas at Pele that have not been explained.

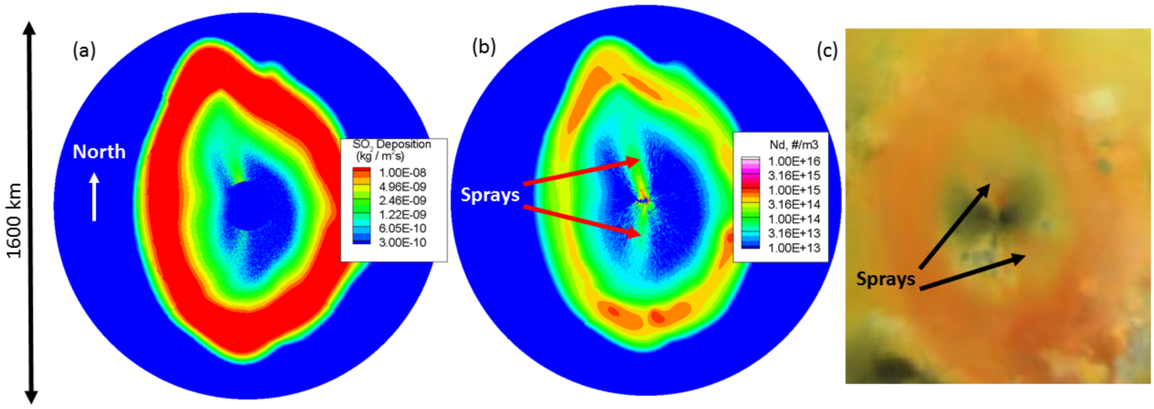

Fig. 23: (a) Recolored gas deposition pattern from Fig. 15a. (b) Number density contours for a constant-altitude slice of the plume ∼500 m above the surface. (c) Galileo image of Pele.

First, the red sprays on the surface of Io to the north and south of the lava lake (but inside of the large ring) did not obviously appear in our simulations of gas deposition. However, the simulations do contain suggestive features which might explain these red sprays with the addition of some plausible assumptions. Fig. 23 presents gas flow near the surface in a slightly different way than the earlier Fig. 15. Fig. 23a is simply a rescaled Fig. 15a, with an exponential color bar instead of a linear one and with saturated gas deposition in the ring. This reveals low-density sprays to the north and south of the lava lake, where deposition exists even if it occurs at a rate an order of magnitude smaller than deposition in the ring. If the observed ring is in fact saturated with SO_2, such that the much lower deposition rate in the sprays can produce nearly as intense of a red coloring on the surface, then our current simulations suffice to explain the observation. Fig. 23b is a constant-altitude slice of gas density in the plume, as in Figs. 11d or 12c, so it is not directly comparable to mass deposition rate (which is the product of near-surface gas density and downward velocity). The densities shown are averages of the gas density in the first ∼1 km above the surface. Here, the jets are much more apparent and are nearly as dense as gas in the canopy where the canopy intersects the surface (at the ring). The difference between Figs. 23a and b is due to the difference in gas velocity in the sprays and in the ring. Gas in the large ring is falling down through the canopy, whereas gas in the sprays is flying outwards from the lava lake nearly parallel to the surface of Io. However, because the gas is this dense at such low altitudes, a small increase in ground elevation over the 500 km between the lava lake and the large red ring would enhance deposition from these gas sprays. If the lava lake is just 2 km lower in elevation than the ring, every gas molecule in the spray near the surface in Fig. 23b would deposit inside of the large ring. The sprays can also be seen Fig. 13c as gas on either side of the vent is much closer to the surface than the gas in Fig. 13a.

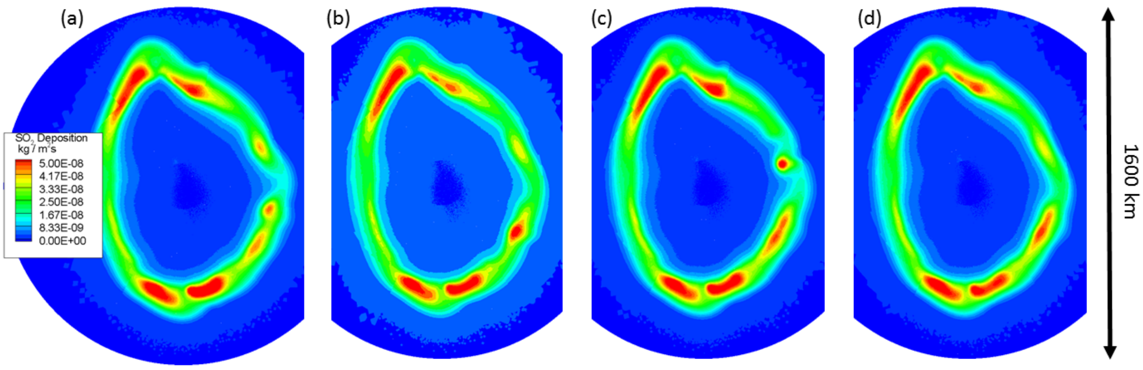

Fig. 24: Gas deposition rates for four nominally identical plume simulations. All plumes are run in the largest domain for 6,000 seconds before sampling the deposition rate over 500 seconds.

We can also suggest an explanation for the observation that the gas ring at Pele sometimes buckles inwards (Geissler et al., 2004). The work presented here has attempted to simulate a steady plume with constant conditions at the lava lake. In some preliminary simulations (not presented) we have seen that small changes to the vent conditions and geometry can produce small changes in the gas deposition. However, even in the simulations presented here the ring is seen to wiggle over time; the gas flow is never quite steady. This is reasonable for a Monte Carlo simulation of a supersonic jet with a high Reynolds number. Small changes in simulation parameters can produce subtle changes in the ring, even for nominally identical gas plumes sampled at the same times (Fig. 24). In simulating the various dust size distribution basis functions used in Section 3.2, nominally identical gas plumes were simulated (to determine the drag on the dust particles). These gas simulations differed only in random number generation and some subtle differences in the structure of the computational grid (due to automatic load-balancing; see Appendix). The various rings in Fig. 24 are all nearly identical in shape and orientation, but red regions of particularly intense deposition differ slightly between simulations. The eastern edge of the ring undergoes the most noticeable change from simulation to simulation, exhibiting sharp buckling in Figs. 24a and c with a region of particularly intense deposition in Fig. 24c at around 3 o'clock. This suggests that some of the unsteadiness in the observations, particularly the buckling seen at the southern edge of the ring, might be explained by occasional slight changes at the lava lake. This also suggests that some of the differences seen between Figs. 15a and 15b may not be entirely attributable to corrections for the non-inertial reference frame.

4.2. Non-Uniform Vent Conditions

In light of the results in Section 3.2.3, where a significant source of error in the best-fit deposition pattern was that our method produced too-dark deposition patterns in the left butterfly wing and too-light patterns in the right butterfly wing, we will now discuss the possibility that non-uniformity in the injection of dust into the plume simulation can explain this imbalance. The different source regions are potentially different in character, with Source A1 being a large lava lake while Sources E and C are smaller, isolated vents, so it is plausible that the mass flux of gas or dust out of the surface is different for each source.

The dust deposition patterns for various size distributions in Fig. 17 show that smaller particles (Figs. 17a-e) preferentially deposit to the west of the lava lake while the largest particles (Fig. 17f) deposit in a nearly symmetric ring. Because smaller particles remain coupled to the gas as plumes rising from each source region begin to interact, the deposition patterns of small particles are sensitive to where those particles are injected into the plume simulation. The gas flow is dominated by emission from Source A1, so light dust injected into the flow to the west of Source A1 will tend to fall to the west of the vent (light dust will have difficulty passing through the oblique shock seen in Fig. 12a and Fig. 13a.). This suggests that almost all small particles injected into the flow at Sources E and C will fall to the west of the vent. If in fact there is very little dust injected into the flow at these sources, our results will overestimate deposition to the west of the vent, which is what was seen in the best-fit deposition patterns.

Let us suppose that half of the dust injected into the plume at Source A1 falls to the west and half to the east, and that all dust (below some size, perhaps) injected into the plume at Sources E and C falls to the west of the vent. Because we inject dust uniformly over the area of our simulated vent regions, we can approximate the effect of turning off dust injection at Sources E and C by weighting dust deposition in the western wing by a ratio of the areas of active regions. Rather than the full areas of Sources E and C and half of the area of Source A1 contributing to dust deposition in the western wing, only half of the area of Source A1 will contribute. This yields a scaling factor of between 0.7 and 0.8 (depending on how we account for the four small, scattered sources to the east of Source A1 which would likely deposit dust to the east of the vent). When simulated dust deposition in the western wing is weighted by this scaling factor before the fitting procedure is performed, the imbalance vanishes on the outer edges of the wings (Fig. 25b) and the fitting error is slightly lower. However, now the eastern wing is noticeably darker than the western wing closer to the vent.

Because the vent is small on the scale of the deposition patterns and because large particles decouple from the gas at low altitudes, the deposition patterns of large particles are only sensitive to the number of particles which are injected into the plume simulation, regardless of their distribution among the source regions. This is why the large particles do not exhibit the same imbalance as the small particles in Fig. 17 -

the large particles are created at the virtual vent with an axisymmetric velocity distribution and are already largely uncoupled from the gas, so they rise and fall nearly ballistically, falling evenly all around the vent. This suggests that we ought not to scale the large dust deposition. In Fig. 25c, we scale only dust smaller than 1,384 nm in diameter, and we see further improvement along with a best-fit deposition pattern with no noticeable east/west anomalies which more closely resembles the pattern obtained by fitting the east and west wings independently (from Fig. 19b). This analysis suggests that Sources E and C are different in character from Source A1, and that much of the error in our best-fit deposition patterns is due to the uniformity of vent conditions in our model. Sources E and C should not be modeled as injecting as much dust (per surface area) into the plume as Source A1.

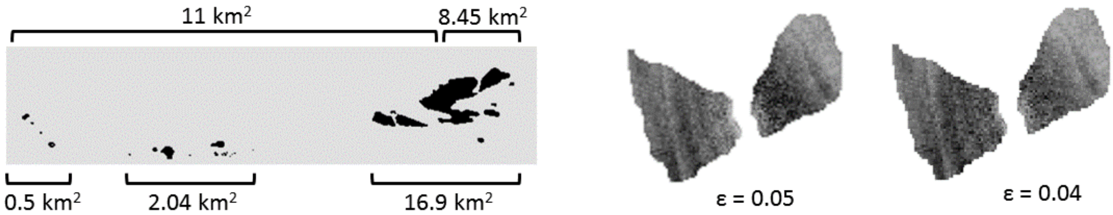

Fig. 25: (a) Sources E, C, and A1, with their individual areas labeled below. Above are the areas assumed to be contributing to dust deposition in the west (11 km^2) and in the east (8.45 km^2). (b) The best-fit deposition pattern obtained after scaling western dust deposition by 0.7. (c) The best-fit deposition pattern obtained after scaling the western deposition of only dust smaller than 1,384 nm in diameter.

4.3. Overlaying of Dust by Gas

While our simulations of dust deposition can produce good fits to the dark coloration of the surface inside of the selected target region (Section 3.2.3), the lack of observed dust deposition (black coloration) outside of the target region needs to be explained, since small dust particles do fall to the surface outside of the target region (Fig. 17). The target region was originally chosen so as to minimize the impact of plume gas deposition on the result, because it is reasonable to assume that significant plume gas deposition would overlay and hide the dust deposition in the ring and in the red sprays north and south of the lava lake. This is supported by the observation of red coloration in these regions, and our simulations (Sections 3.1.3 and 4.1) show how SO_2 might preferentially deposit where the surface appears red.

The mechanism by which dust is concealed by gas deposition may be complicated. With a steady plume, resurfacing is an ongoing process. Dust particles that produce the black coloration on the surface will have a lower albedo than other surface materials on Io like SO_2 frost, and likely lower thermal inertia as well (supported by modeling in Walker et al., 2012). Until black dust particles are covered by an optically thick layer of frost, they will absorb sunlight during the day and heat up to a greater extent than will the white, yellow, or red materials that cover the surface of Io near Pele. Walker et al. (2012) find that "non-frost" surfaces overlaid by only a thin layer of condensed gas (SO_2, mostly) heat up rapidly at sunrise, causing the release of the trapped gas in a puff (the "dawn atmospheric enhancement"). This presents a puzzle about the overlaying of black dust at Pele by red/yellow plume material. Why is Pele not black everwhere that dust deposits, since SO_2 has difficulty sticking to warm dust? When Pillan erupted, leaving a black spot in the eastern part of Pele's ring, how did the red ring re-establish itself?

One possibility is that the gas plume deposits so much material over a single night that an optically thick layer of frost can form on top of a dark dust deposit. However, the plume would have to be much denser than the one simulated here in order to produce an optically thick layer of frost overnight. The inner diameter of the large red ring is about 700 km while its outer diameter is about 1000 km. SO_2 ice has a density of about 1900 kg/m^3 (this depends on morphology and may be closer to 1500 kg/m^3), and Nash et al. (1980) give 0.25 mm as the thickness at which a layer of fine-grained SO_2 frost becomes optically thick in experiments. The plume simulated here has a gas mass flow rate of 10,700 kg/s. If, as in our simulations, this is 100% SO_2, it would take the plume 0.6 years to deposit an optically thick layer of frost in the ring. Very little SO_2 frost will deposit during any particular night, and so SO_2 deposition consistent with observed column densities does not seem to be capable of overlaying dust.

However, because Pele is believed to contain as much as 30% S_2 by molar fraction (Spencer et al., 2000), overlaying of black ash by S_2 and products of S_2 may be possible, and products of S_2 could account for the red coloration anyway (McEwen and Soderblom, 1983). This can occur even if the deposition rate is slow since species other than SO_2 frost have much lower vapor pressures at dayside temperatures (this is why SO_2 dominates the sublimation atmosphere). S_2 has the same molecular weight as SO_2, and so generally tracks the simulated SO_2 plume (Zhang, 2004). If the density and optical properties of sulfur on the surface are similar to those used above for SO_2 frost (an assumption we make for lack of good constraints on these properties), it should take around 1.9 years to deposit an optically thick layer of sulfur if Pele is 30% S_2 and is continuously erupting. This will take longer if there is less S_2 in the plume or if there are periods of reduced or no activity. Once the red sulfur layer becomes sufficiently thick, the higher thermal inertia and albedo of the solid material relative to loosely-packed dust grains may allow SO_2 frost to build up as well, since frost-covered surfaces will not reach the high temperatures of dusty surfaces during the day.

The predicted 1.9 years to overlay dust may be tested by comparison to Galileo observations of the eruption of Pillan. This eruption occurred over a short time and deposited black material which overlaid Pele's red ring. This black spot was then seen fading slowly over the course of subsequent observations, which supports our earlier conclusion that Pele could not be laying down sufficient SO_2 to produce an optically thick layer upon the dust in a single night. Geissler (2004) discusses changes in Pele and Pillan over time, and the observations used show Pillan's black spot appearing in late 1997. By the end of 1999, the spot had faded considerably, and was no longer visible by the end of 2000. This overlaying took between two and three years, which is consistent with overlaying of dust by only S_2 from a mostly continuously-active Pele which contains 20-30% S_2. Jessup et al (2007) mostly find lower S_2/SO_2 ratios, from 0.02 to 0.1, but there appears to be significant variation over time. They estimate a range between 0.08 and 0.3 for a 1999 observation (during the time when Pillan's deposition was being covered over by Pele) and then a range from 0.2 to 0.31 for a 2004 observation.

4.4. Multiple Types of Particles

In Section 3.2.3, we found best-fit dust size distributions in terms of linear combinations of basis functions spanning 20 nm to 10 µm (and we were only able to fit from about 60 nm to 10 µm because smaller particles were overlaid by the gas ring). The best-fit size distribution derived from the uniform basis functions in Fig. 18c has a mean of 125 nm, weighted by number. This compares well with the observations of Jessup and Spencer (2012), who used the Hubble Space Telescope to find mean particle sizes of between about 50 and 100 nm in the Pele plume. Our mean is larger, but this can be explained by our necessary exclusion from consideration of smaller particles. By fitting an analytic function to our distribution, we can extend it to smaller particles and obtain a measure of mean particle size which can be directly compared to the Jessup and Spencer observation. The log-normal distributions shown here were obtained using Matlab's non-linear least squares fitting function with a very low tolerance and from a wide variety of starting guesses.

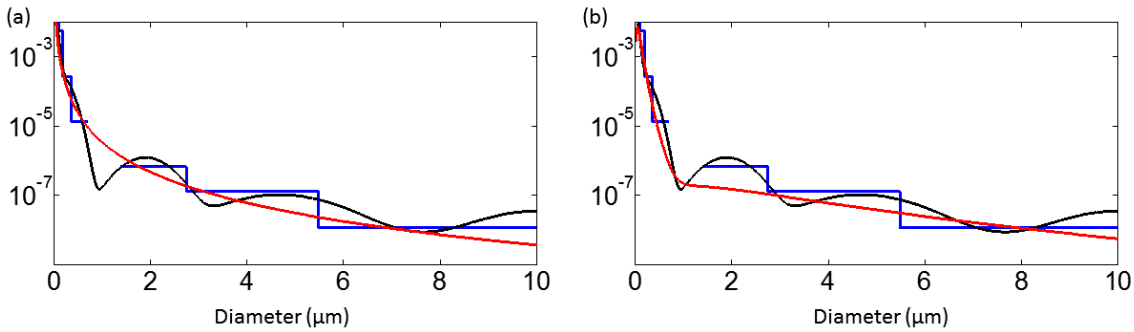

Fig. 26: (a) Comparison of best-fit size distributions to a single log-normal distribution given by $f = \frac{1}{d\sigma\sqrt{2\pi}} e^{-\frac{(\ln d - \mu)^2}{2\sigma^2}}$, where d is the particle diameter in nanometers, μ is -7.51 nm, and σ is 2.81 nm, and the entire distribution is scaled to sum to 1 over the range 20-10,000 nm. (b) Comparison of best-fit size distributions to the weighted sum of two log-normal distributions given by $f = \frac{\alpha}{d\sigma_1\sqrt{2\pi}} e^{-\frac{(\ln d - \mu_1)^2}{2\sigma_1^2}} + \frac{\beta}{d\sigma_2\sqrt{2\pi}} e^{-\frac{(\ln d - \mu_2)^2}{2\sigma_2^2}}$ where α is 0.6422, μ_1 is 4.25 nm, σ_1 is 0.623 nm, β is 5.939×10^{-4}, μ_2 is 7.75 nm, and σ_2 is 0.797 nm. As with earlier plots of size distributions, 'Fraction' represents the fraction of particles with each integer nanometer diameter.

No single normal or log-normal distribution does a good job of capturing the behavior of the best-fit distributions in Fig. 18c due to the gap or drop at 1 µm. Ignoring the gap, reasonably good agreement is found between our best-fit size distributions and a log-normal distribution with a μ parameter of -7.51 nm and a σ parameter of 2.81 nm (Fig. 26a). This distribution has an extremely small mean (less than 1 nm) because it becomes very large near 0.

We get a more plausible result when we fit our combination of basis functions with the weighted sum of two log-normal distributions. One distribution with a μ parameter of 4.25 nm and a σ parameter of 0.623 nm and another with a μ parameter of 7.75 nm and a σ parameter of 0.797 nm can be combined (weighting the first by a factor of 0.6422 and the second by a factor of 5.939×10^{-4}) to obtain the function shown in Fig. 26b. This function has a mean of about 88 nm, which is much closer to the finding of Jessup and Spencer, and also better captures the drop at $\sim$1 µm.

This suggests that the true size distribution of dust particles in the plume is likewise the sum of two distributions, which indicates that there may be two different mechanisms of particle creation. Earlier (Section 2.4) we discussed a boiling oatmeal analogy to explain why large particles might have significant tangential velocity at the lava lake, while smaller particles might have a different creation mechanism involving small filaments of lava rather than large-scale spattering. These two different mechanisms would naturally result in two different particle size distributions.

We also note here that a coincidence is seen for particles in the plume at a particular diameter. As discussed just above, our best-fit size distributions yield a gap or trough at $\sim$1 µm. The deposition patterns produced by dust distributions cease contracting towards the vent at $\sim$1 µm; the radius of the deposition pattern in Fig. 17e is almost the same as that in Fig. 17f. It is plausible that these effects are related, but the nature of the connection is unclear.

5. Conclusions

Three-dimensional simulations of Pele were performed which were able to reproduce many observed features of the gas and dust flow. Using a source based on observations of the lava lake at Pele, our DSMC code produced an asymmetric gas plume with an appropriate canopy height and a deposition ring that closely matched observations. The simulations were able to explain the plume and ring as a result of low-altitude interactions between gas flows expanding from different discrete source regions and the overall geometry of the lava lake. The simulated deposition rate of plume gas in the ring was found to be able to explain observations of Pele slowly overlaying Pillan.

Simulated dust in the plumes showed how particles encode information from the lava lake even as the gas flow expands and becomes diffuse. Simulated dust was used to produce a best-fit size distribution in an attempt to determine the actual size distribution of ash particles at Pele. The best-fit distribution was found to be relatively insensitive to several model assumptions, and the relative amounts of dust particles of diameters $>\sim$60 nm were constrained. Line-of-sight integrated column densities of dust particles were compared to Voyager observations, and we found that $\leq\sim$20 nm particles must be present in very large quantities relative to larger particles.

We developed a model of the flow just above the surface of Io and showed how a nearly-uniform "virtual vent" can develop from a pattern of cracks or holes in the crust of a large lava lake. We found that the lake could be well-approximated as infinite in expanse at low altitudes, and showed how gas rising from the lava accelerates dust particles as a function of their size. We used this model to reduce the number of free parameters for the dust at the virtual vent.

Future work should implement the effects of plasma bombardment on the plume. Plasma should heat the canopy, and might transfer significant momentum as well, and it is important to verify that simulated deposition continues to agree with observation. Plumes should also be integrated into simulations of Io's sublimation atmosphere, where they can influence and be influenced by pressure-driven winds.

- We show how the geometry of the lava lake at Pele produces the ovoid red ring on Io.
- Gas expands to the north and south because of gas-dynamic effects at low altitudes.
- Ash particles fall in distinctive patterns depending on their size.
- We find a size distribution for ash particles which explains the black fans at Pele.
- Ash preserves information about the flow from the very surface of the lava lake.

6. Appendix: Computational Grid and Load-Balancing

The three-dimensional simulation of complex plumes, with such hugely varying length scales and mean free paths, presented some new computational challenges. Methods for automatically determining processor boundaries and the grid structure within processors were very important for setting up and performing the computations efficiently. The computational domain is a section of a spherical shell, bounded by surfaces of constant latitude, longitude, and altitude. Processor boundaries also lie along latitude and longitude lines, with each extending from the surface to the top of the domain. Each processor is typically allocated 44,000 cells. The grid of cells is uniform in latitude, longitude, and altitude within each processor. The distribution of this budget of cells to each spherical coordinate direction is automatically chosen so as to minimize the largest cell size (in any dimension) anywhere in the processor. If this procedure results in a cell with less than a predefined minimum cell size, the cell allowance is reduced and the number of cells to allot to each spherical coordinate direction is recalculated. A uniform grid in latitude and longitude in each processor is suitable for this problem because the resolution is allowed to vary between processors such that processors which take up less volume achieve finer resolutions, and the volume of a processor is tied to the local flow density, integrated in altitude (discussed below). This results in cell sizes which scale very nearly with mean

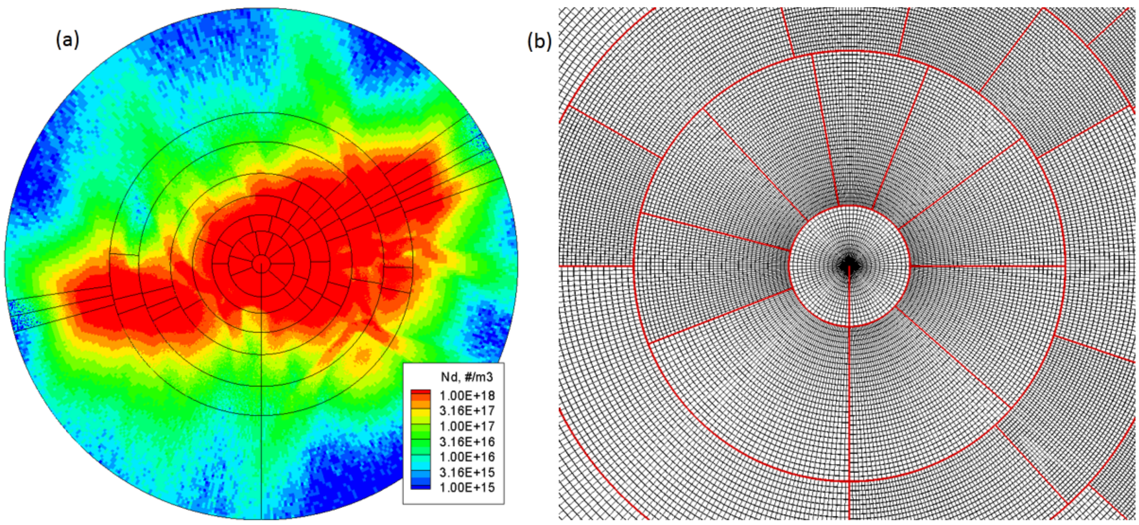

Fig. 27: (a) Number density contours for flow in a constant-altitude slice 1 km above Source A1, with black processor boundaries visible. The simulation was performed on 64 processors one polar cap and seven rings of nine processors each. Over the course of the simulation the processor boundaries adjusted so as to balance the number of particles in each processor, and here processors are seen to be concentrated near 2:00 and 9:00, following the shape of the red high-density region. Three processors in the outer ring simulate a large fraction of the total simulation domain, because density in the outer regions is generally very low. (b) A close-up of the polar cap processor and the innermost ring. Processor boundaries are in red and cell boundaries are in black. The grid structure (in latitude and longitude) is visible and the effect of the singularity at the axis is seen in the cells in the polar cap.

free paths in each processor, in latitude and longitude, although cell sizes do not vary with altitude (except across stages, which are simulated separately).

For the plume simulations in this paper, the source of the plume is located near the pole of the spherical domain. This has the advantage of placing a roughly radially symmetric flow in a roughly radially symmetric grid. Generally, we desire smaller cells nearer the central axis of the plume where densities are higher, but uniform decomposition in longitude produces a near-singularity in the grid at the axis. As the cell sizes shrink, it becomes difficult to keep enough simulated molecules in each cell to resolve collisions, and statistics-driven instabilities can occur (Zhang 2004). We mitigate this by using a non-uniform processor distribution that allows the placement of a single processor at the pole spanning 360 degrees in longitude and covering a very narrow range of latitudes. By allowing this polar cap processor a small number of cells, the cells remain acceptably large along the polar axis, but, because the processor does not extend out far in latitude, the cells do not grow unacceptably large along the processor's outer edge (Fig. 27b).

Load-balancing is an important consideration because the simulation can only proceed at the speed of the slowest processor. Most computer time is taken up by collisions between simulated gas molecules, the number of which tends to increase as the number of particles in a processor increases. A straightforward method of load-balancing that roughly approximates collision-based balancing is simple molecule balancing, i.e. balancing with the goal of placing an equal number of molecules in each processor (all of which have nearly identical numbers of cells).

While a precomputed set of processor boundaries is acceptable for many problems, it is not suitable for many unsteady flows. At the beginning of a plume simulation, all of the molecules are very near the center of the domain. After the plume's initial expansion, there are a large number of molecules around the periphery of the domain. After the canopy shock forms, most of the molecules are at mid-latitudes. With static load-balancing based on the steady plume, the early time steps would take just as long to compute as the later time steps, and the middle time steps would take longer than either. Dynamic load-balancing is used to compute the transient stages of the simulation quickly. At intervals, a crude (perhaps 1,000 $\times$ 1,000) set of bins is used to map where the molecules in the domain are in latitude and longitude. This allows the domain to be split into a set number of rings in latitude, where each ring has roughly equal numbers of molecules. Then each ring is split up into a set number of processors in longitude, where each processor has a roughly equal share of the molecules in its ring. In this way a given number of processors can be moved around over the course of a simulation such that the number of molecules in a particular processor at any time is roughly equal to the total number of molecules divided by the number of processors.

7. Acknowledgments

This work was supported by a NASA Earth and Space Science Fellowship under Grant number NNX12AN78H and by NASA-PATM grant NNX08AE72G. Computations were performed on supercomputers at the Texas Advanced Computing Center.

References

[1] Bird, G. A., 1994. Molecular gas dynamics and the direct simulation of gas flows.

[2] Boyd, I. D., Burt, J. M., 2003. Development of a two-way coupled model for two phase rarefied plume flows.

[3] Burgi, P.-Y., Caillet, M., Haefeli, S., 2002. Field temperature measurements at erta'ale lava lake, ethiopia. Bulletin of volcanology 64 (7), 472–485.

[4] Davies, A., Keszthelyi, L., Lopes-Gautier, R., McEwen, A., Smythe, W., Soderblom, L., Carlson, R., 1999. Thermal signature, eruption style and eruption evolution at pele and pillan patera, on io. In: Lunar and Planetary Institute Science Conference Abstracts. Vol. 30. p. 1462.

[5] Davies, A. G., 2007. Volcanism on io. Volcanism on Io, by Ashley Gerard Davies, Cambridge, UK: Cambridge University Press, 2007 1.

[6] Davies, A. G., Veeder, G. J., Matson, D. L., Johnson, T. V., 2012. Charting thermal emission variability at pele, janus patera and kanehekili fluctus with the¡ i¿ galileo¡/i¿ nims io thermal emission database (nited). Icarus 221 (1), 466–470.

[7] Geissler, P., McEwen, A., Keszthelyi, L., Lopes-Gautier, R., Granahan, J., Simonelli, D., 1999. Global color variations on io. Icarus 140 (2), 265–282.

[8] Geissler, P., McEwen, A., Phillips, C., Keszthelyi, L., Spencer, J., 2004. Surface changes on io during the galileo mission. Icarus 169 (1), 29–64.

[9] Geissler, P., McMillan, M., 2008. Galileo observations of volcanic plumes on io. Icarus 197 (2), 505–518.

[10] Geissler, P. E., Goldstein, D. B., 2007. Plumes and their deposits. In: Io After Galileo. Springer, pp. 163–192.

[11] Howell, R. R., Lopes, R., 2011. Morphology, temperature, and eruption dynamics at pele. Icarus 213 (2), 593–607.

[12] Jessup, K. L., Spencer, J., Yelle, R., 2007. Sulfur volcanism on io. Icarus 192 (1), 24–40.

[13] Jessup, K. L., Spencer, J. R., 2012. Characterizing ios pele, tvashtar and pillan plumes: Lessons learned from hubble. Icarus 218 (1), 378–405.

[14] Lellouch, E., Belton, M., De Pater, I., Paubert, G., Gulkis, S., Encrenaz, T., 1992. The structure, stability, and global distribution of io's atmosphere. Icarus 98 (2), 271–295.

[15] McDoniel, W., October 2013. Cracks in a lava lake: Boundary conditions for io's pele plume. Direct Simulation Monte Carlo 2013: Theory, Methods, and Applications (DSMC13).

[16] McDoniel, W., Goldstein, D., Varghese, P., Trafton, L., Buchta, D., Freund, J., Kieffer, S., Levin, D. A., Wysong, I. J., Garcia, A. L., 2011. Simulating irregular source geometries for ionian plumes. In: AIP Conference Proceedings-American Institute of Physics. Vol. 1333. p. 1157.

[17] McEwen, A. S., Keszthelyi, L., Geissler, P., Simonelli, D. P., Carr, M. H., Johnson, T. V., Klaasen, K. P., Breneman, H. H., Jones, T. J., Kaufman, J. M., et al., 1998. Active volcanism on io as seen by galileo ssi. Icarus 135 (1), 181–219.

[18] McEwen, A. S., Soderblom, L. A., 1983. Two classes of volcanic plumes on io. Icarus 55 (2), 191–217.

[19] Moore, C., Goldstein, D., Varghese, P., Trafton, L., Stewart, B., 2009. 1-d dsmc simulation of io's atmospheric collapse and reformation during and after eclipse. Icarus 201 (2), 585–597.

[20] Moore, C. H., Walker, A. C., Goldstein, D. B., Varghese, P. L., Trafton, L. M., Parsons, N., Levin, D. A., 2012. Dsmc simulations of the plasma bombardment on ios sublimated and sputtered atmosphere. In: 50th AIAA Aerospace Sciences Meeting, Nashville, TN. Jan. 9th–12th. AIAA-2012-0560.

[21] Nash, D., Fanale, F., Nelson, R., 1980. So2 frost: Uv-visible feflectivity and io surface coverage. Geophysical Research Letters 7 (9), 665–668.

[22] Patankar, S., 1980. Numerical heat transfer and fluid flow. CRC Press.

[23] Prem, P., Artemieva, N., Goldstein, D., Varghese, P., Trafton, L., 2014. Transport of water in a transient impact-generated lunar atmosphere. Icarus.

[24] Radebaugh, J., McEwen, A. S., Milazzo, M. P., Keszthelyi, L. P., Davies, A. G., Turtle, E. P., Dawson, D. D., 2004. Observations and temperatures of io's pele patera from cassini and galileo spacecraft images. Icarus 169 (1), 65–79.

[25] Smith, B. A., Soderblom, L. A., Johnson, T. V., Ingersoll, A. P., Collins, S. A., Shoemaker, E. M., Hunt, G., Masursky, H., Carr, M. H., Davies, M. E., et al., 1979. The jupiter system through the eyes of voyager 1. Science 204 (4396), 951–972.

[26] Spencer, J. R., Jessup, K. L., McGrath, M. A., Ballester, G. E., Yelle, R., 2000. Discovery of gaseous s2 in io's pele plume. Science 288 (5469), 1208–1210.

[27] Stewart, B., 2010. Numerical simulations of the flow produced by a comet impact on the moon and its effects on ice deposition in cold traps.

[28] Stewart, B. D., Pierazzo, E., Goldstein, D. B., Varghese, P. L., Trafton, L. M., Moore, C. H., 2009. Parallel 3d hybrid continuum/dsmc method for unsteady expansions into a vacuum. In: 47th AIAA Aerospace Sciences Meeting, Orlando, Florida, AIAA. Vol. 266.

[29] Strom, R., Schneider, N., 1982. Volcanic eruption plumes on io. In: Satellites of Jupiter. Vol. 1. pp. 598–633.

[30] Strom, R. G., Schneider, N. M., Terrile, R. J., Cook, A. F., Hansen, C., 1981. Volcanic eruptions on io. Journal of Geophysical Research: Space Physics (1978–2012) 86 (A10), 8593–8620.

[31] Walker, A. C., Gratiy, S. L., Goldstein, D. B., Moore, C. H., Varghese, P. L., Trafton, L. M., Levin, D. A., Stewart, B.,

2010. A comprehensive numerical simulation of ios sublimation-driven atmosphere. Icarus 207 (1), 409–432.

[32] Walker, A. C., Moore, C. H., Goldstein, D. B., Varghese, P. L., Trafton, L. M., 2012. A parametric study of ios thermophysical surface properties and subsequent numerical atmospheric simulations based on the best fit parameters. Icarus 220 (1), 225–253.

[33] Williams, D. A., Keszthelyi, L. P., Crown, D. A., Yff, J. A., Jaeger, W. L., Schenk, P. M., Geissler, P. E., Becker, T. L., 2011. Volcanism on io: New insights from global geologic mapping. Icarus 214 (1), 91–112.

[34] Zhang, J., 2004. Simulation of gas dynamics, radiation and particulates in volcanic plumes on io.

[35] Zhang, J., Goldstein, D., Varghese, P., Gimelshein, N., Gimelshein, S., Levin, D., 2003. Simulation of gas dynamics and radiation in volcanic plumes on io. Icarus 163 (1), 182–197.

[36] Zhang, J., Goldstein, D., Varghese, P., Trafton, L., Moore, C., Miki, K., 2004. Numerical modeling of ionian volcanic plumes with entrained particulates. Icarus 172 (2), 479–502.

[37] Zolotov, M. Y., Fegley, B., 2000. Eruption conditions of pele volcano on io inferred from chemistry of its volcanic plume. Geophysical research letters 27 (17), 2789–2792.

[38] Zolotov, M. Y., Fegley Jr, B., 2001. Chemistry and vent pressure of very high-temperature gases emitted from pele volcano on io. In: Lunar and Planetary Institute Science Conference Abstracts. Vol. 32. p. 1474.